

Topological edge state transfer via topological adiabatic passage

Chong Wang,^{1,2,*} Xiu Gu,^{1,2,*} Shu Chen,³ and Yu-xi Liu^{1,2,†}

¹*School of integrated circuits, Tsinghua University, Beijing, 100084, China*

²*Frontier Science Center for Quantum Information, Beijing, China*

³*Beijing National Laboratory for Condensed Matter Physics,
Institute of Physics, Chinese Academy of Sciences, Beijing 100190, China*

(Dated: August 3, 2023)

The study of quantum state transfer has led to a variety of research efforts utilizing quantum simulators. By exploiting the tunability of the qubit frequency and qubit-qubit coupling, a superconducting qubit chain can simulate various topological band models. In our study, we demonstrate that a spin-up state can be transported along a topological qubit chain by modulating the coupling strengths and the qubit frequencies. We show that the Hilbert space of the qubit chain can be restricted to the subspace of two edge states in this process, while the Hamiltonian degenerates into a two-state Landau-Zener (LZ) model. Furthermore, we prove that the state transfer process in this topological qubit chain is equivalent to the topological adiabatic passage of the LZ model. With this analysis, we generalize the state transfer approach from single-qubit Fock states to two-qubit Bell states.

I. INTRODUCTION

The discovery of topological insulators [1] triggered extensive studies in topological phases of matter. Topological insulators, topological superconductors, and topological semimetals are just a few examples. It is well known that the topological power stems from its global geometric properties characterized by topological invariants. The topological protections can result in many potential applications, for example, topological quantum computation [2], in which the non-Abelian states of matter are used to encode and manipulate quantum information in a nonlocal manner. These nonlocal global states are topologically protected, and are more robust against the decoherence of qubit states or local impurities of quantum computational devices.

Topological phenomena were first demonstrated in crystals and other condensed matter systems. Recently, the study for topological physics has been applied to photonic systems, ultracold atoms, and ultracold gases in optical lattices [3–5]. These systems enhance the possibility to create and probe new topological phases. Furthermore, inspired by quantum computing, in which the qubits and their couplings can be controlled or tuned, topological physics is studied via quantum computational devices. The reason is twofold. First, some exotic topological states, which are not easy to find in natural systems, may be created and probed by artificially designing and fabricating on-demand quantum computational devices. Second, some topological states, which are experimentally difficult to create in natural systems, may be simulated via quantum simulators [6].

The simplest model exhibiting topological characters is the Su-Schrieffer-Heeger (SSH) model [7–10]. It has been

extensively studied by theorists [11–14] and attracted different experimental platforms (e.g., in Refs. [15–21]). For example, in cold atoms, the topological invariant of the one dimensional band, also known as the Zak phase [22], was measured [18]. Because of the bulk-edge correspondence, the band invariant is associated with the existence of edge states. The edge signal is not easy to resolve from the bulk in the real space lattice of cold atoms. Recently in the momentum space of cold atoms, the dynamics of edge states was probed [19]. The quantized transport of particles, known as the Thouless pump [23], was also demonstrated in cold atoms by modulating the on-site potential and coupling strength of the SSH model [20, 21].

Recently, topological physics is explored through superconducting quantum circuits (or superconducting artificial atoms) [24–26]. Unlike natural atoms, these circuits can be fabricated with well-tailored characteristic frequencies and other parameters. The exquisite control of superconducting quantum circuits makes it possible to simulate topological band models on a single superconducting qubit. This is achieved by mapping the bulk momentum space of a topological band model, onto the parameter space of a spin in an external magnetic field [27]. The Berry phase was first measured in a single superconducting qubit [28–32]. Via Berry phase, topological invariants characterizing the band properties were also measured [33–35]. The space-time inversion symmetric topological semimetal [36] and topological Maxwell metal bands [37] were also simulated in a single superconducting qubit circuit. Experimental efforts are now directed to large scale of superconducting qubits. As an initial step towards realizing fractional quantum Hall effect, anyonic fractional statistical behavior is emulated in superconducting circuits with four qubits coupled via a quantized microwave field [38]. Also, directional transport of photons was observed on a unit cell formed by three superconducting qubits [39]. In this design, qubits play the role of the lattice sites, whereas the synthetic topological materials are made of photons. There are var-

* These authors contributed equally to this work.

† yuxiliu@mail.tsinghua.edu.cn

ious interesting theoretical proposals to study topological physics based on superconducting circuits [40–47].

Here, rather than using microwave photons coupled by superconducting qubits, we propose to simulate topological physics with a chain of coupled superconducting qubits. As a simulator of spin physics, the coupled superconducting qubits are widely studied [48–52]. For instance, quantum annealing was demonstrated experimentally on an Ising spin chain comprised of eight superconducting flux qubits [50]. Due to the improved controllability and fabrication technique of superconducting circuits, it becomes accessible to fabricate tens of qubits with various types of couplings. The qubit frequency and qubit-qubit coupling strengths can all be tuned in situ, making the whole superconducting qubit chain versatile enough to simulate topological models [10, 53, 54]. Inspired by the studies in other systems (e.g., in Refs. [15–21]), we here study topological edge states and pumping by constructing the SSH model and Rice-Mele model [9, 10] using gap-tunable flux qubit circuits [55–58].

The paper is organized as follows. In Section II, we briefly introduce the topological qubit chain constructed of gap-tunable flux qubits. This spin chain model can be mapped to SSH model or Rice-Mele model when restricted to single excitation subspace. In Section III, we show that the single-qubit edge state can be transported from one end of the chain to the other end by adiabatic pumping. We theoretically analyze this pumping process and propose one optimized pumping protocol. In Section IV, we generalize the state pumping protocol to two-qubit state transfer with a trimer Rice-mele model. In Section V, we summarize our results and further discuss possible demonstration on topological physics using superconducting qubit circuits. For the completeness of the paper, we also give a detailed superconducting circuit analysis for the spin chain in the appendix.

II. TOPOLOGICAL QUBIT CHAIN WITH SUPERCONDUCTING QUBITS

As schematically shown in Fig. 1(a), we study a superconducting quantum circuit, in which $2N$ identical superconducting qubits are coupled to form a chain with alternating coupling strengths. That is, the coupling strength between the qubit (marked in green) on the odd sites and its right neighbor (marked in orange) is a , while the coupling strength between the qubit (marked in orange) on the even sites is coupled to its right neighbor (marked in green) with an amplitude of b . It is well known that the coupling constants a and b between qubits can be designed to be tunable in superconducting qubit circuits by using, e.g., additional coupler, variable qubit frequency, detuning between qubits, or frequency matching [59–70].

In principle, the coupled qubit chain can be constructed by any type of superconducting qubits, e.g., flux qubits [71, 72], transmon [73], xmon [74] and

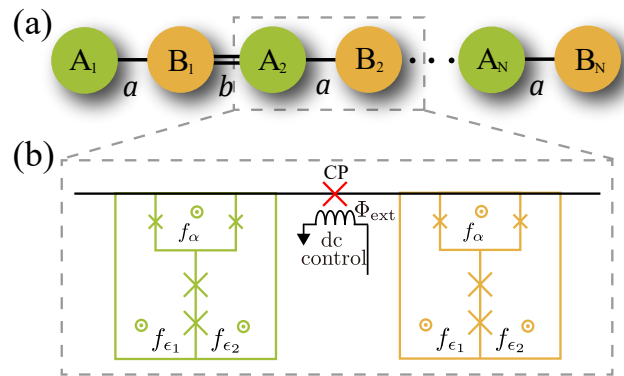


FIG. 1. (a) Schematic diagram of a one-dimensional topological qubit chain. Each unit cell hosts two qubits, labeled as A_n and B_n separately. The coupling strengths between A_n and B_n are staggered, denoted as a and b . Each qubit can also be labeled by one increasing numerical index j from left to right. (b) Realization of the qubit chain with gap-tunable flux qubits. Each qubit contains two basic superconducting circuit elements, i.e., the Josephson junction and the inductance. Two adjacent qubits are coupled through a tunable coupler (CP). The qubit-qubit coupling can be tuned via an external magnetic flux Φ_{ext} with a dc control. The signs \odot denote that the magnetic fluxes are directed outside. We use reduced magnetic fluxes $f_\alpha = \Phi_\alpha/\Phi_0$, $f_{\epsilon_1} = \Phi_1/\Phi_0$, and $f_{\epsilon_2} = \Phi_2/\Phi_0$. Here Φ_α , Φ_1 and Φ_2 are the magnetic fluxes through the three small loops of the qubit. Φ_0 is the flux quanta. The frequency of the gap-tunable flux qubit can be tuned via the magnetic flux through the α -loop or main loop, thus both the qubit frequencies and the couplings in the qubit chain are tunable.

gmon [75, 76]. Compared with the qubits [73–76], the gap-tunable flux qubit circuit [55–58] has negligibly small population leakage from the first excited state to other upper states when the two lowest energy levels are operated as the qubit near the optimal point. Also the frequency of the gap-tunable flux qubit can be tuned via the magnetic flux through the α -loop or main loop. Moreover, the gap-tunable flux qubit has better coherent time. Thus, for concreteness of the discussions and as an example, we first assume that each qubit in the chain is implemented by a gap-tunable flux qubit circuit [55, 57, 77], as schematically shown in Fig. 1(b) and is further explained in Appendix A. Through the detailed study below for the chain of the gap-tunable flux qubit circuit, we will give the comparative summary for the chain formed by other types of superconducting qubits in the discussions.

The qubit chain consists of N unit cells, and each unit cell contains two sublattices labeled as A_n and B_n with $n = 1, 2, \dots, N$. The couplings between adjacent qubits are staggered, denoted as a and b . Here we relabel each qubit in the chain by one increasing index j from A_1 to B_N , then the Hamiltonian of such a qubit chain can be

mapped to the Rice-Mele model. The pumping can be realized if the staggered potentials and the coupling strengths in the Hamiltonian can be modulated. Such time modulations for qubit frequencies and coupling strengths can be realized in superconducting qubit circuits as discussed in Appendix B.

If we only consider the single-excitation states, as discussed in Section II, the time-dependent Hamiltonian in Eq. (B11) with qubit frequency modulations can be reduced to the Hamiltonian of the Rice-Mele model [10, 79] as

$$H_{\text{RM}} = \sum_n [a(t)A_n^\dagger B_n + b(t)A_n^\dagger B_{n-1} + \text{H.c.}] + u(t) \sum_n (A_n^\dagger A_n - B_n^\dagger B_n), \quad (6)$$

where A_n^\dagger (B_n^\dagger) is the particle creation operator on the site A (B) in the n th cell, $a(t)$ and $b(t)$ are the time dependent coupling strengths, $u(t)$ is the staggered potential. This Rice-Mele Hamiltonian can be continuously deformed along the time-dependent pump sequences given by $u(t)$, $a(t)$ and $b(t)$. In superconducting quantum circuits, this can be done by varying the magnetic fluxes through the couplers and the α loops of the superconducting qubits.

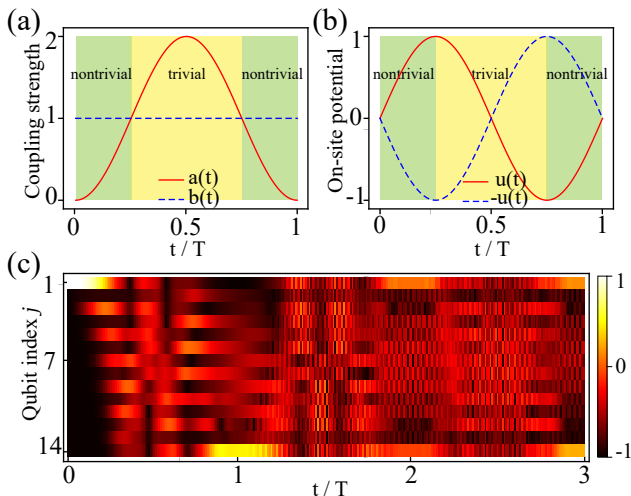


FIG. 2. (a) The coupling strengths a and b versus time t . (b) The on-site potentials u and $-u$ versus time t . (c) Time evolution of the particle distributions $\langle \sigma_j^z \rangle$ for the qubit chain of $2N = 14$ qubits. The time-dependent pump sequence is defined in Eq. (7), with $T = 100$. The color from dark-red to bright-yellow represents the particle distribution $\langle \sigma_j^z \rangle$ varying from -1 to 1 .

For example, as shown in Fig. 2, we can demonstrate the topological pumping by simply choosing the coupling strengths $a(t)$ and $b(t)$ as well as the on-site potential $u(t)$

as

$$\begin{aligned} a(t) &= 1 - \cos\left(\frac{2\pi t}{T}\right), \\ b(t) &= 1, \\ u(t) &= \sin\left(\frac{2\pi t}{T}\right). \end{aligned} \quad (7)$$

where T is the variation period of these parameters. Figures 2(a) and (b) show the time-dependent coupling strengths and on-site potentials versus time t during one period. The numerical simulation of the dynamical evolution of the qubit chain, as shown in Fig. 2(c), is solved using ordinary differential equation solver based on backward differentiation (BDF) formulas [80]. The result shows that the soliton edge state can indeed be transferred from one end of the chain to the other end within one pumping cycle. To ensure the adiabatic limit, we set $T = 100$. The chain is initialized in the all spin-down state. To prepare the left edge state, the first qubit is flipped by a π pulse of the applied magnetic flux through the main loop of the qubit. However, this pumping process somehow can't last more than one circle.

The instantaneous spectrum of the Hamiltonian in Eq. (6) is plotted as a function of t in Fig. 3(a). The black-solid lines represent the bulk states and the color-dashed lines represent the edge states. According to the quantum adiabatic theorem (berry's article), if the adiabatic approximation holds during the pumping circles, the system will stay in the same eigenstate as the prepared initial state. With the increasing of the on-site potential, two degenerate edge states separate from each other and develop into two branches. As shown in Fig. 3(b), the state on point b of the upper branch is mostly located on the left end of the chain. Therefore, if the initial state is prepared as the left edge state, it will adiabatically evolve following the upper branch as shown in the red-dashed line in Fig. 3(a).

The wave functions of six particular points on the upper branch are plotted in Fig. 3(b) to (g). For the first pumping cycle, the result shown in Fig. 2(c) is consistent with the adiabatic limit in Fig. 3. The soliton first diffuses as the left edge state with vanishing amplitudes on the even sites. Then it is pushed into the bulk occupying both even and odd sites. After that, it reappears as the right edge state with vanishing amplitudes on the odd qubits. At the end of the first pumping cycle, as shown in Fig. 3(f), the right edge state refocuses on the right end qubit. The soliton edge state is already transferred from the left end to the right end before the crossing point. As shown in Fig. 3(g), the eigenstate in point g is the same in point f. Indeed, after this crossing point, the evolving route follows the red-dashed line from point f to point g, which is also verified in Fig. 2(c). Apparently, the evolution of the state around the level crossing does not follow the traditional adiabatic theorem, which will be discussed later in Section III B.

Through the wave functions at points b to f in Fig. 3, we have shown how a left edge state is adiabatically

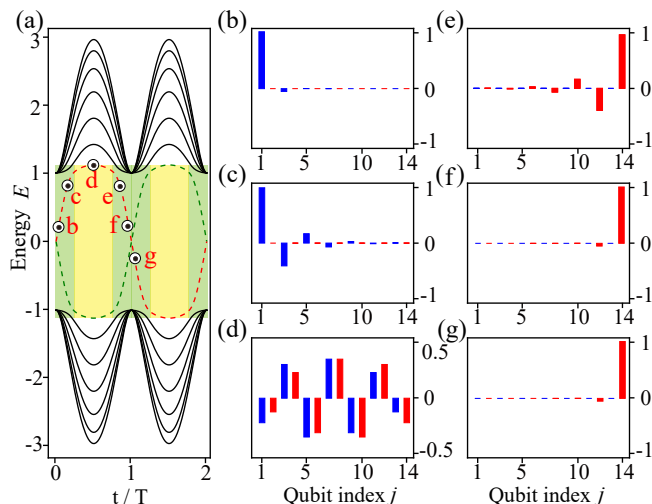


FIG. 3. (a) Instantaneous spectrum of the Hamiltonian in Eq. (6) with the pumping sequence defined in Eq. (7). The chain consists of $2N = 14$ qubits. When $t > 0$, the on-site potential will relieve the degeneracy of two edge states and break the degenerate energies into two branches, as shown in the red- and green-dashed lines. Five particular states on the upper branch are chosen as b, c, d, e, f, and g. The corresponding wave functions are shown in (b) to (g).

pumped to the right during a pumping cycle. It is seen that the state occupies the left edge and right edge equally in point d. We denote this to be the transition point. Combining Fig. 2 and Fig. 3, we can summarize two principles to achieve the edge state transfer. The first one is that, as shown in Fig. 2(b), the on-site potential $u(t)$ must change sign at the transition point, i.e., $t = T/2$. The second one is that, to insure the adiabaticity, the energy gap must be opened between two branches during the state transfer process, i.e., the coupling strengths can't be zero around the transition point, as shown in Fig. 2(a). Based on these two principles, we can easily redesign some other time-dependent pump sequences to achieve QST.

In our pump result, only the edge mode is occupied initially, while the lower band is empty. However, in the cold atom experiments [20, 21], all the lower band is filled with the atoms, while the upper band is empty. During a pumping cycle, each atom in the valence band is moved to the right by a single lattice constant. Or equivalently, the number of pumped particles through the cross section is one. This is determined by the Chern number of the associated band [10]. By promoting the periodic time t to the wave-number, the adiabatic pump sequence in one dimension is equivalent to two-dimensional insulators.

B. Topology of the pumping process

When the on-site potentials u are equal to 0, the former Rice-Mele model in Eq. (6) is reduced to the SSH model.

As discussed in Section. C, for a standard SSH model in the nontrivial topological phase, i.e., $|a| < |b|$, two existing topological edge states are denoted as $|L\rangle$ and $|R\rangle$. While the coupling coefficients a and b are positive real numbers, two edge states can be expressed as

$$|L\rangle = \Xi \sum_n \lambda^{n-1} |e_{2n-1}\rangle \quad (8)$$

and

$$|R\rangle = \Xi \sum_n \lambda^{L-n} |e_{2n}\rangle \quad (9)$$

where $\Xi = \sqrt{(1-\lambda^2)/(1-\lambda^{2N})}$ is the normalization factor and $\lambda = -a/b$ is the ratio of the coupling coefficients. In the nontrivial topological phase, the two edge states $|L\rangle$ and $|R\rangle$ hybridize under the Hamiltonian H to an exponentially small amount, meanwhile, the couplings between the edge states and the bulk states are much exponentially smaller. With a good approximation using adiabatic elimination of the other bulk states [10], we can investigate the state transfer process in the subspace of $\{|L\rangle, |R\rangle\}$. This idea of restricting the Hilbert space of the dynamic process can also be generalized to the Rice-Mele model [81–83]. As for the our system shown in Eq. (6), the matrix elements of the effective Hamiltonian in this subspace take the following forms as

$$\langle L|H|L\rangle = -\langle R|H|R\rangle = u, \quad (10)$$

$$\langle L|H|R\rangle = \langle R|H|L\rangle = \Xi^2 a \lambda^{L-1}. \quad (11)$$

Hence the effective Hamiltonian can be written as

$$H = \begin{pmatrix} u & g \\ g & -u \end{pmatrix}, \quad (12)$$

where $g = \Xi^2 a \lambda^{L-1}$ is the effective coupling strength between two edge states. Thus, we transform the complicated many-body problem into a two-state quantum dynamics.

For a two-state Landau-Zener (LZ) model [84] shown in Eq. (12), we can characterize the adiabatic state transfer processes based on the topology of the eigenenergy surfaces [85]. The eigenenergies of the effective Hamiltonian in Eq. (12) are

$$E_{\pm} = \pm \sqrt{u^2 + g^2}. \quad (13)$$

The two eigenenergy surfaces can be drawn as a dirac cone shown in Fig. 4(b), and the two energy bands intersect at the critical point $u = 0$ and $g = 0$. There are two basic types of topological passages depending on whether the adiabatic evolution path goes through the critical point.

To illustrate the differences between these two passages, we particularly choose two paths with the same start point and end point as shown in the solid lines in

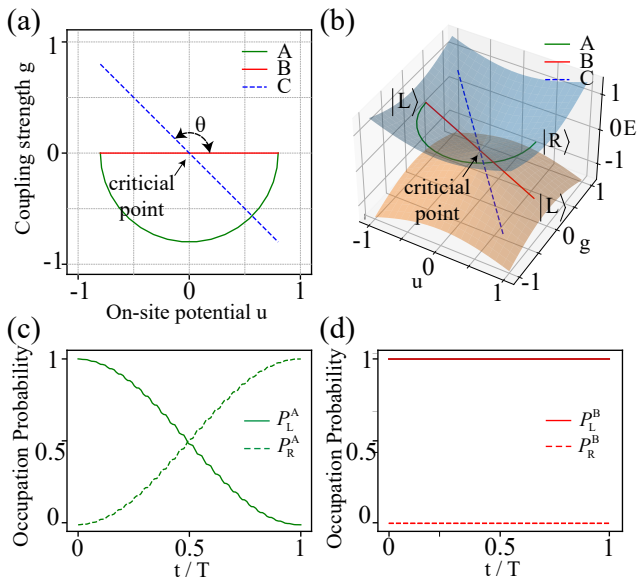


FIG. 4. (a) Three paths shown in the parameter space of on-site potential u and coupling strength g . (b) The energy spectrum of the two-level system. Different parameter paths of the same start point and end point can lead to different evolution paths. (c) Time evolution of state occupation along path A. (d) Time evolution of state occupation along path B.

Fig. 4(a). The green path A is an arc and can be described as

$$u = \alpha \cos\left(\frac{\pi t}{T} - \pi\right), g = \alpha \sin\left(\frac{\pi t}{T} - \pi\right). \quad (14)$$

Due to the quantum adiabatic theorem [86, 87], if the parameters of the quantum system are changed slowly enough, it will remain in its instantaneous eigenstate. As shown in Fig. 4(b), if the initial state is prepared as $|L\rangle$ on the upper branch, the adiabatic following of the path A can induce the complete state transfer from $|L\rangle$ to $|R\rangle$. This adiabatic process is verified with numerical simulation as shown in Fig. 4(c). The red path B is a straight line and can be described as

$$u = \alpha \left(\frac{2t}{T} - 1\right), g = 0. \quad (15)$$

As shown in Fig. 4(b), the two bands merge at the critical point in the section of $g = 0$, and hence the adiabatic following here should be handled more carefully. Notice that if $g = 0$, the two states $|L\rangle$ and $|R\rangle$ are decoupled from each other. Therefore, as the parameter u changes continuously, the system will remain in the same state. This evolution process is verified with numerical simulation as shown in Fig. 4(d).

More generally, an arbitrary straight path through the critical point can be described as

$$u = \alpha \left(\frac{2t}{T} - 1\right), g = \tan(\theta) u \quad (16)$$

as shown in the blue-dashed line in Fig. 4(a). The Hamiltonian of this path C can be written as

$$H = \frac{u}{\cos\theta} \begin{pmatrix} \cos\theta & \sin\theta \\ \sin\theta & -\cos\theta \end{pmatrix}. \quad (17)$$

Eigenstates of the Hamiltonian in Eq. (17) have the form

$$\begin{bmatrix} |\uparrow\rangle \\ |\downarrow\rangle \end{bmatrix} = \begin{pmatrix} \cos\frac{\theta}{2} & \sin\frac{\theta}{2} \\ \sin\frac{\theta}{2} & \cos\frac{\theta}{2} \end{pmatrix} \begin{bmatrix} |L\rangle \\ |R\rangle \end{bmatrix}. \quad (18)$$

These two eigenstates are time-independent and the corresponding eigenenergies are $E = \pm u/\cos\theta$. Therefore, the Hamiltonian in the basis of $|\uparrow\rangle$ and $|\downarrow\rangle$ can be written as

$$H = \frac{u}{\cos\theta} \begin{pmatrix} 1 & 0 \\ 0 & -1 \end{pmatrix}. \quad (19)$$

From this perspective, the two states $|\uparrow\rangle$ and $|\downarrow\rangle$ are decoupled from each other. If the initial state is prepared as $|\uparrow\rangle$ or $|\downarrow\rangle$, the system will remain in the same state over time. In the Fig. 4(b), we show the state on the path C initially prepared as $|\uparrow\rangle$ evolves from the upper branch to the lower branch across the critical point. Thus, *the adiabatic passage around the critical point support the state transfer, while the adiabatic passage through the critical point leaves the system in the same state.*

As for the state transfer proposal in Section III A, the parameters of the effective Hamiltonian can be derived from Eqs. (7), (10) and (11). The path of this adiabatic passage in parametric space is shown in Fig. 5(a). The whole evolution process can be divided into three stages denoted as red-solid line, green-dashed line and blue-solid line, individually. The solid lines represent the topological nontrivial region and the dashed line represents the topological trivial region. As shown in Fig. 5(b), in the first stage, the on-site potentials rise up and the system keeps the same state, i.e., $|L\rangle \rightarrow |L\rangle$. In the second stage, the state evolves from the left edge into the bulk and then reaches to the right edge, i.e., $|L\rangle \rightarrow \text{bulk} \rightarrow |R\rangle$. In the third stage, the on-site potentials decrease to 0 and the system maintains the same state, i.e., $|R\rangle \rightarrow |R\rangle$. Therefore, after one pumping cycle, the state is transferred from the left edge to the right edge.

As discussed before, the approximation of adiabatic elimination of bulk states works only in the topological nontrivial region. In the topological trivial region, the couplings between the edge states and the bulk states can not be ignored, and the dashed lines of the second stage in Fig. 5 are not the real evolution path. Nevertheless, the energy bands in the topological trivial region are separated from each other as shown in Fig. 3, and the adiabatic following is still feasible in this region. Therefore, after the first stage, the state is confirmed to evolve from the left edge into the bulk. The three-stage description of the state transfer process is still applicable.

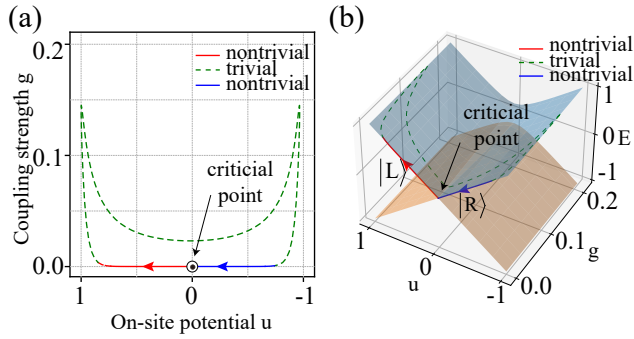


FIG. 5. (a) The path of the adiabatic passage of the effective Hamiltonian in the parametric space. (b) Evolution path of the adiabatic passage in the energy spectrum.

C. Optimization of the pumping cycle

With the analysis above, it is easy to conclude that the inaccuracy of the pumping does not come from the crossing energy levels, but from the close energy bands in the topological trivial region. Hence we need to adjust the system parameters to get larger gaps between the adiabatic passage and other bulk states in our advanced pump protocol as compared with Fig. 3.

As shown in Fig. 3, in the first topological nontrivial region, the energy of the edge state increases with the on-site potential before the edge state joins the bulk. Thus the first clew is to decrease the amplitude of the on-site potential. Here we choose the on-site potential as $u(t) = 0.25 * \sin(2\pi t/T)$. As shown in Fig. 6(a), the maximum energy of the edge state indeed decreases in the topological nontrivial region, but the edge state still joins the bulk hereafter in the topological trivial region due to the topological phase transition. Therefore the second clew is to avoid the topological phase transition so that the edge state can be well isolated from the bulk. Here apart from the modified on-site potential $u(t)$, we further choose the coupling strength a as $a(t) = 0.5 * [1 - \cos(2\pi t/T)]$, so that the relation $a < b$ can be conserved during the whole pumping cycle and the system will stay in the topological nontrivial region. As shown in Fig. 6(b), the adiabatic passage is well isolated with other bulk states during the whole quantum state transfer process.

In Fig. 6(c), the numerical simulation of the qubit chain's dynamical evolution is well resolved. With the parameters above, the initial state prepared on the first site of the chain can be perfectly transferred to the last site in a pumping cycle. This pumping process can last for many pumping cycles with high fidelity. Therefore, we can indeed optimize our pumping protocol using the topological analysis in Section III B.

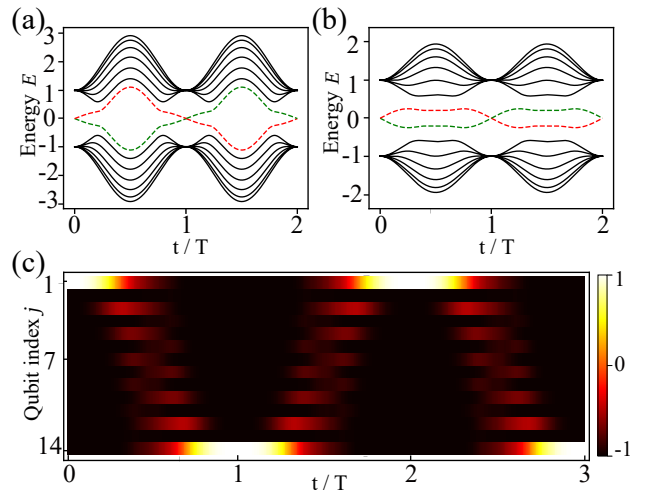


FIG. 6. (a) The energy spectrum of the chain with $u(t) = 0.25 * \sin(2\pi t/T)$. (b) The energy spectrum of the chain with $u(t) = 0.25 * \sin(2\pi t/T)$ and $a(t) = 0.5 * [1 - \cos(2\pi t/T)]$. (c) Time evolution of the particle distributions $\langle \sigma_j^z \rangle$ for the qubit chain. The color from dark-red to bright-yellow represents the particle distribution $\langle \sigma_j^z \rangle$ varying from -1 to 1 .

IV. TWO-QUBIT BELL STATE PUMPING IN A TRIMER RICE-MELE MODEL

Above from the perspective of the traditional adiabatic theorem, we have exhibited a more ordinary way to understand the thouless pumping in 1D Rice-Mele model. With this comprehensible explanation, we can easily generalize the state transfer protocol to a trimer Rice-Mele qubit chain.

As shown in Fig. 7, the trimer Rice-Mele model is a periodic qubit chain with the unit cell of three sites. The Hamiltonian of the trimer RM model can be written as

$$H_{\text{TRM}} = \sum_n [aA_n^\dagger B_n + bB_n^\dagger C_n + cC_n^\dagger A_{n+1} + \text{H.c.}] + \sum_n [uA_n^\dagger A_n + vB_n^\dagger B_n + wC_n^\dagger C_n] \quad (20)$$

where A_n^\dagger , B_n^\dagger and C_n^\dagger are the particle creation operators on the sites A, B and C in the n th unit cell. a , b and c are the coupling strengths between each sites. u , v and w are the staggered potentials on sites A, B and C.

When the on-site potentials are chosen to be 0, the trimer Rice-Mele model in Eq. (20) is reduced to the extended SSH3 model. As shown in Ref. [88], there are generally two different cases for the topological characterization of this SSH3 model. One is the mirror symmetry case ($a = b$) and the other is the none mirror symmetry case ($a \neq b$). For the convenience of discussion, we only consider the mirror symmetry case hereafter. In this case, the Hamiltonian exhibits a band gap closing when $a = b = c$, and the edge states emerge at this gap closing point in the thermodynamic limit [88].

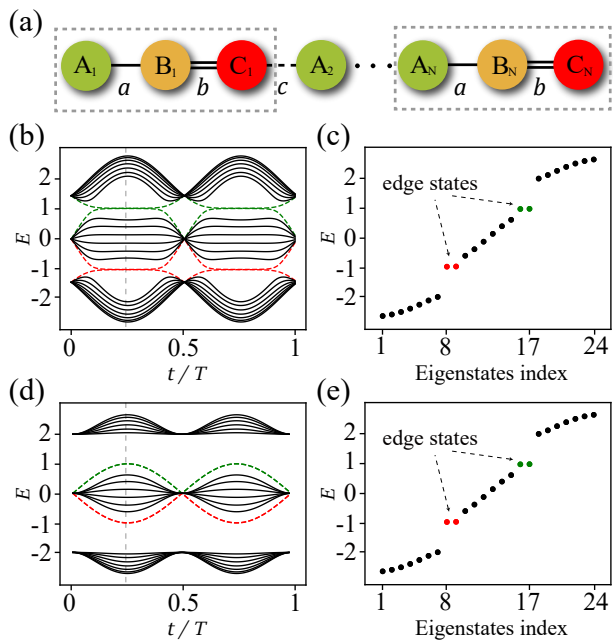


FIG. 7. (a) Schematic diagram for a trimer qubit chain. The 3 identical sites in each unit cell are denoted by green circle, orange circle and red circle. a and b denote the intracell coupling strengths, while c denotes the intercell coupling strength. (b) The energy spectrum with respect to the intercell coupling $c(t)$ (unit cells $N = 8$). The green dashed line and red dashed line represent the edge modes. (c) The eigenstates distribution on the black dashed line in (b). (d) The energy spectrum with respect to the intracell couplings. (e) The eigenstates distribution on the black dashed line in (d).

In Fig. 7(b), we plot the energy spectrum with respect to the intercell coupling c , which depends on the time t . The coupling strengths are chosen as

$$a = b = 1, c(t) = 2 \sin\left(\frac{2\pi t}{T}\right). \quad (21)$$

The edge states only exist in the region $c(t) > a$, where the SSH3 model has the nontrivial topology. We can easily notice that there are 4 edge states divided by 2 gaps. The edge states in each gap are degenerate when $c(t) \gg a$. Specifically, the eigenstates distribution at $c(t) = 2$ is plotted in Fig. 7(c). The two pairs of degenerate edge states are clearly shown in red dots and blue dots.

Considering the former Thouless pumping protocol, we can plot another energy spectrum with respect to the intracell couplings as shown in Fig. 7(d). The coupling strengths are chosen as

$$a(t) = b(t) = \sin\left(\frac{2\pi t}{T}\right), c = 2 \quad (22)$$

where the intracell couplings are time-dependent and the intercell coupling c is constant. With the parameters

above, the system remains in the topologically trivial region, so the edge states are degenerate all along. We can also clarify the degenerate edge states with the eigenstates distribution in Fig. 7(e).

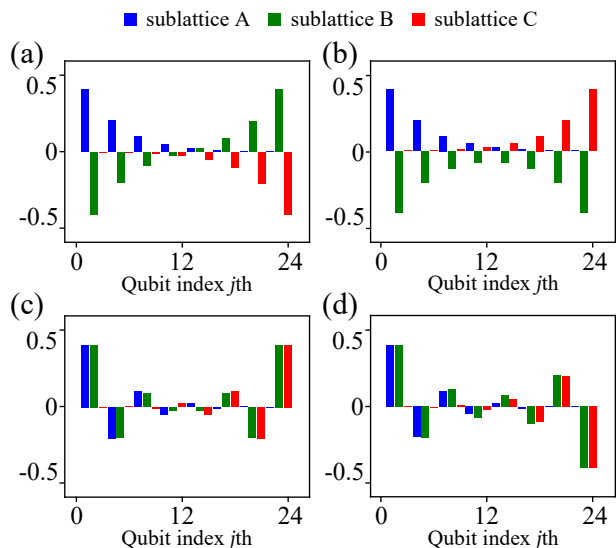


FIG. 8. The wave functions of four hybridized edge states exhibited in Fig. 7(e). (a) and (b) show the hybridized edge states in the lower gap. (c) and (d) show the hybridized edge states in the upper gap.

In a finite size SSH3 model, there must be an exponentially small overlap between the left and the right edge states. Thus the wave functions of the eigenstates in the bulk band gaps must be the superpositions of the left and the right edge states. In the nontrivial topological phase, four existing edge states of the SSH3 model can be denoted as $|L_{\pm}\rangle$ and $|R_{\pm}\rangle$. The localized eigenfunctions in the lower and upper band gaps can be individually expressed as $(|L_{-}\rangle \pm |R_{-}\rangle)/\sqrt{2}$ and $(|L_{+}\rangle \pm |R_{+}\rangle)/\sqrt{2}$. In Fig. 8, we plot the wave functions of the four hybridized edge states. The pattern of these hybridized wave functions is just the same as the original SSH model in Section C. Therefore, we can easily derive the forms of the four edge states as

$$|L_{\pm}\rangle = \Xi \sum_n (\mp\lambda)^{n-1} \left(\frac{|e_{3n-2}\rangle \pm |e_{3n-1}\rangle}{\sqrt{2}} \right) \quad (23)$$

and

$$|R_{\pm}\rangle = \Xi \sum_n (\mp\lambda)^{L-n} \left(\frac{|e_{3n-1}\rangle \pm |e_{3n}\rangle}{\sqrt{2}} \right) \quad (24)$$

where $\Xi = \sqrt{(1-\lambda^2)/(1-\lambda^{2N})}$ is the normalization factor and $\lambda = a/c$ is the ratio of the coupling coefficients.

A. The state pumping process in the subspace of edge states

The whole analysis of the trimer Rice-Mele model above is in the mirror symmetric case, i.e. $a = b$. Therefore the Hamiltonian in Eq. (20) can be rewritten as

$$H_{\text{TRM}} = \sum_n [a (A_n^\dagger B_n + B_n^\dagger C_n) + c C_n^\dagger A_{n+1} + \text{H.c.}] + \sum_n [u A_n^\dagger A_n + v B_n^\dagger B_n + w C_n^\dagger C_n]. \quad (25)$$

Following the lead of the former analysis in Section III B, we can firstly rewrite the system Hamiltonian in the subspace of $\{|L_\pm\rangle, |R_\pm\rangle\}$. As shown in Fig. 7, when $v \neq 0$, the upper edge states are well isolated from the lower edge states, so we can further divide this subspace into two individual subspaces $\{|L_+\rangle, |R_+\rangle\}$ and $\{|L_-\rangle, |R_-\rangle\}$. As for our trimer Rice-Mele system shown in Eq. (20), the matrix elements of the effective Hamiltonian in the edge state subspace take the following forms as

$$\langle L_+ | H | L_+ \rangle = a + \frac{u+v}{2}, \langle R_+ | H | R_+ \rangle = a + \frac{v+w}{2} \quad (26)$$

$$\langle L_+ | H | R_+ \rangle = \langle R_+ | H | L_+ \rangle = \frac{L(a+v) + a}{2} \Xi^2 (-\lambda)^{L-1} \quad (27)$$

$$\langle L_- | H | L_- \rangle = -a + \frac{u+v}{2}, \langle R_- | H | R_- \rangle = -a + \frac{v+w}{2} \quad (28)$$

$$\langle L_- | H | R_- \rangle = \langle R_- | H | L_- \rangle = \frac{L(a+v) + a}{2} \Xi^2 \lambda^{L-1} \quad (29)$$

Thus the effective Hamiltonian in the edge state subspace can be described as

$$H = \begin{pmatrix} H_+ & \\ & H_- \end{pmatrix}, \quad (30)$$

where H_+ and H_- represent the Hamiltonian in the upper subspace $\{|L_+\rangle, |R_+\rangle\}$ and the lower subspace $\{|L_-\rangle, |R_-\rangle\}$, respectively. Hence H_+ and H_- are given by

$$H_+ = \begin{pmatrix} \frac{u}{2} & g_+ \\ g_+ & \frac{w}{2} \end{pmatrix} + \left(a + \frac{v}{2}\right) I \quad (31)$$

and

$$H_- = \begin{pmatrix} \frac{u}{2} & g_- \\ g_- & \frac{w}{2} \end{pmatrix} - \left(a - \frac{v}{2}\right) I, \quad (32)$$

where I is identity matrix, g_+ and g_- are the coupling strengths between the edge states, given by

$$g_\pm = \frac{L(a+v) + a}{2} \Xi^2 (\mp\lambda)^{L-1} \quad (33)$$

The effective Hamiltonians H_+ and H_- have the same form as in Eq. (12). Thus we can achieve the quantum state transfer via the same adiabatic passages.

B. Two-qubit Bell state transfer via the trimer Rice-Mele model

As discussed before, the adiabatic quantum state transfer process needs to begin in the topological non-trivial region, i.e. $a \ll c$. In the first stage, the on-site potential of the left edge should be much larger than that of the right edge, i.e. $u \gg w$. With the evolution of the system, the on-site potentials u and w of the left and right edge states exchange their values slowly. At some point, there will be a moment that these two potentials reach the same value, i.e. $u = w$. To avoid the degeneracy of the edge states, the system should be in the topological trivial region near this point, i.e. $a \simeq c$. Afterwards the potentials of two edge states totally exchanges their values and the system returns back to the topological trivial region. Thus the coefficients of the Hamiltonian along the state transfer process are denoted as

$$\begin{aligned} a &= b = 1 - 0.9 * \cos\left(\frac{2\pi t}{T}\right), \\ c &= 1, v = 2, \\ u &= 1 + \cos\left(\frac{\pi t}{T}\right), w = 1 - \cos\left(\frac{\pi t}{T}\right), \end{aligned} \quad (34)$$

where T is the variation period of these parameters.

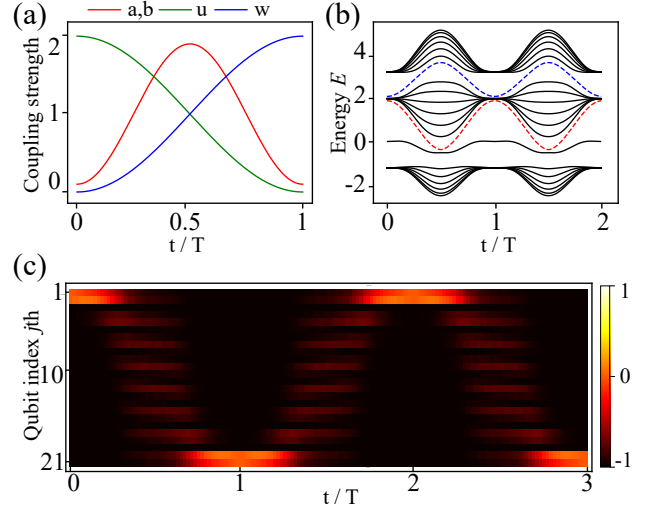


FIG. 9. (a) The coupling strengths a, b and on-site potentials u, w versus time t . (b) The energy spectrum of the trimer Rice-Mele chain, which contains $3L = 21$ qubits. (c) Time evolution of the particle distributions $\langle \sigma_j^z \rangle$ for the qubit chain. The time-dependent pump sequence is defined in Eq. (34), with $T = 1000$. The color from dark-red to bright-yellow represents the particle distribution $\langle \sigma_j^z \rangle$ varying from -1 to 1 .

Figures 9(a) show the time-dependent coupling strengths and on-site potentials versus time t during one period. The initial states are prepared as two-qubit Bell states, i.e., $(|e_1\rangle \pm |e_2\rangle)/\sqrt{2}$ in this qubit chain.

As shown in Figures 9(b), the two selected topological adiabatic passage are denoted as blue-dashed and red-dashed lines, which can be used to transfer the Exchange-symmetric and Exchange-antisymmetric Bell states. The numerical simulations of the dynamical evolution of the qubit chain prepared in a Bell state is shown in Fig. 9(c). The result shows that the symmetric Bell state can indeed be transferred from one end of the chain to the other end within one pumping cycle. The result of the antisymmetric Bell state is not shown, for the purpose of simplification, because it is identical to the prior example. To ensure the adiabatic limit, we set $T = 1000$. As show in the simulation, this pumping process can last for more than three circles. Therefore, we can indeed achieve the edge state pumping in a trimer Rice-Mele model via topological adiabatic passages.

V. DISCUSSIONS AND CONCLUSIONS

A. experimental feasibility

Let us now further discuss the experimental feasibility. The qubit-qubit coupling in flux qubit circuit can be tuned from 0 to 60 MHz [75, 76]. Therefore, in our proposal, the state transfer process needs about 10 μs for 7 unit cells for the gap-tunable flux qubit circuit. The coherence time of qubit is about 10-100 μs [89, 90], thus it is quite reasonable for execute state transfer process with our protocol. Our proposal can also be realized in other superconducting qubit circuits, e.g., transmon qubit, which has long coherence time, tunable coupling and frequency modulation. The disadvantage is that anharmonicity is not very good for the transmon qubits, thus the population leakage needs to be considered. In table I, we list the advantage and disadvantage for two different type of qubit to realize our proposal. We note that the topological magnon insulator states have been experimentally demonstrated in a superconducting circuit with 5 transmon qubits [91]. Thus it is not very difficult to further study the topological physics using large scale of superconducting quantum circuits with current technology.

QT	CT	TC	FM	Anh
Flux qubit	microseconds	Yes	Yes	Good
Transmon	Several tens seconds	Yes	Yes	Not good

TABLE I. Comparisons of the flux and transmon qubits for constructing a qubit chain to realize our proposal. Here, QT, CT, TC, FM and Anh denote Qubit Type, Coherence Time, Tunable Coupling, Frequency modulation, and anharmonicity, respectively.

As for measurements, we can couple the qubit chain dispersively to a microwave resonator. This means the qubits and resonator are detuned in frequency so they

do not exchange energy. Applying a microwave pulse at the bare resonator frequency, the pulse will experience a frequency shift and accumulate a phase shift [92–95]. By measuring the phase shift of the reflected or transmitted probe pulse, we can infer the state of the qubit.

We note that our qubit chain can be used to implement pumping using one-dimensional Aubry-Andre-Harper (AAH) model [53, 54, 96], which is related to the well-known Hofstadter butterfly problem [97] in two dimensions. In our proposal, the AAH model can be obtained through the Hamiltonian in Eq. (B1), in which the frequency ω of the j th qubit needs to be modulated as $\omega \cos(2\pi j\alpha + t/T)$, where α is a rational (irrational) number. However, the qubit-qubit coupling strengths need to be changed to uniform, i.e., $a = b$. Experimentally, this can be realized by fabricating the chain of coupled superconducting flux qubits with uniform coupling strength, the frequency modulation can be done by applying the magnetic fields through the main loop of each qubit. However, if the coupling strengths of superconducting qubit chain are tunable, then we need only to tune all coupling strengths so that they equal to each other. We further note that the pumping of an edge state based on AAH model was realized in quasicrystals [98]. Recently, the Hofstadter butterfly spectrum was observed in a chain of nine coupled gmon qubits [99].

We mention that the qubit chain can also be constructed using circuit QED system [25, 26], where the qubit-qubit coupling can be mediated by the cavity fields. In this case, the cavity fields works as quantum couplers, thus the qubit-qubit coupling can be obtained by eliminating the cavity field with assumption that the qubits and the cavity fields are in the large detuning.

B. Conclusions

We have proposed to simulate topological phenomenon using a gap-tunable superconducting-qubit chain, in which the Hamiltonian is equivalent to the SSH model when the total excitations of the qubit chain is limited to one. The spin-up injection at the localized edge state is robust against fluctuations, which can be used to store quantum information. We further show an equivalence of the Rice-Mele model can be realized with the time modulated frequencies and the coupling strengths of the qubit chain, and the adiabatic pumping of an edge state can be realized in this time modulated qubit chain. In our numerical simulation, we take a larger number of the qubits in the chain, e.g., 7 unit cells. However, we find that the topological phenomena can also be demonstrated in such chain with even smaller qubit number, e.g., 4 unit cells. We also find that the localization can become more strong with the increase of the qubit number of the chain.

In summary, superconducting quantum circuits can be artificially designed according to the purpose of the experiments. In particular, the qubit frequencies and qubit-qubit couplings can be easily modulated or tuned. This

opens many possibilities to simulate or demonstrate various topological physics of matter on demand with artificial designs. We demonstrate that a spin-up state prepared in the one edge of a topological qubit chain can be transferred to the other edge of the chain. This stater transfer process can be interpreted by restricting the Hilbert space of the Hamiltonian into the subspace of the edge states. Thus the hamiltonian of the chain can degenerate to a two-state LZ model, and the state transfer process in the long qubit chain can be easily understood with the adiabatic passage in the LZ model. With this comprehension, we have designed a new approach to achieve the two-qubit Bell state transfer in a trimer Rice-Mele model. Our proposal can also be expended to other tunable quantum system.

ACKNOWLEDGMENTS

Y.X.L. acknowledges the support of the National Basic Research Program of China Grant No. 2014CB921401 and the National Natural Science Foundation of China under Grant No. 91321208. S.C. is supported by the National Key Research and Development Program of China (2016YFA0300600), NSFC under Grants No. 11425419, No. 11374354 and No. 11174360.

Appendix A: Gap-tunable flux qubit

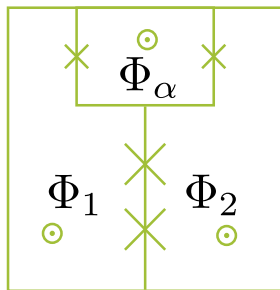


FIG. 10. Schematic diagram for the gap-tunable flux qubit. The magnetic flux threading the α -loop is denoted by Φ_α . Φ_1 and Φ_2 denote magnetic fluxes through the left and right of the main loop. The signs \odot denote that the magnetic fluxes are directed outside.

Let us now briefly summarize the main properties of the gap-tunable flux qubit circuit [55–57], which is a variation of a three-junction flux qubit [71, 72]. It replaces the smaller junction in the three-junction flux qubit with a superconducting quantum interference device (SQUID), which is equivalent to a single junction. The SQUID loop is called as α -loop. An externally controllable flux Φ_α applied to the α -loop can change the Josephson energy of the smaller junction, and the ratio between the larger junctions and the smaller junction is

also tunable. This directly results in tunable tunneling between two potential wells of the flux qubit [71] and the time modulated frequency of the qubit by applying ac magnetic flux through the α -loop. To keep Φ_α from affecting the biased flux threading the main loop, a gradiometric design is adopted. In such design, the central current of the three-junction flux qubit is split into two opposite running currents through two small loops. The magnetic fluxes generated by these two currents cancel each other in the main loop, thus independent control over both fluxes in α -loop and main loop is guaranteed. Magnetic fluxes Φ_1 and Φ_2 , applied to two small loops of the qubit, are used to tune the potential well energy of the qubit. Because both the tunneling and the potential well energies can be tuned in the gap-tunable flux qubit, we have a fully controllable Hamiltonian. Below, we use reduced magnetic fluxes $f_\alpha = \Phi_\alpha/\Phi_0$, $f_{\epsilon_1} = \Phi_1/\Phi_0$, and $f_{\epsilon_2} = \Phi_2/\Phi_0$. Here Φ_0 is the flux quanta.

We define the flux difference between the two loop halves of the gradiometer as $f_\epsilon = f_{\epsilon_1} - f_{\epsilon_2}$. At the optimal point where $f_\epsilon = 0$, the low-frequency effect of the environmental magnetic flux reaches minimum, and the two lowest-energy states of the flux qubit are the super-currents states $\pm I_p$ circulating in opposite directions in the f_ϵ loop. In the persistent current states basis, e.g., the anticlockwise current state $|\odot\rangle$ and clockwise current state $|\ominus\rangle$, the Hamiltonian of the qubit takes the form (detailed in Appendix D)

$$H = \frac{1}{2}(\epsilon \sigma_x + \delta \sigma_z), \quad (\text{A1})$$

where σ_z and σ_x are Pauli matrices, the parameter δ is the tunneling energy between the states of two potential wells and can be tuned by the reduced magnetic flux f_α . By changing f_α and f_ϵ , the energy bias $\epsilon(f_\epsilon, f_\alpha) = 2f_\epsilon \Phi_0 I_p(f_\alpha)$ can be tuned to zero, where the qubit is its optimal point and insensitive to magnetic flux noise to first order. That is, the qubit Hamiltonian in Eq. (A1) can be fully controlled by both f_α and f_ϵ . Moreover, in contrast to the three-junction qubit, in which the transition frequency δ is fixed at the optimal point, the gap-tunable flux qubit allows us to control the qubit frequency without affecting the bias point, that is, δ can be tuned by f_α even at the optimal point with $f_\epsilon = 0$. This is demonstrated in detail in the appendix. Moreover, if a time-dependent magnetic flux with the frequency ω_0 is applied to the α -loop, a time-dependent longitudinal coupling [100, 101] Hamiltonian $\lambda_z \sigma_z \cos(\omega_0 t)/2$ with the coupling constant λ_z between the qubit and external field should be included, then the qubit Hamiltonian in Eq. (A1) becomes into

$$H' = \frac{1}{2}(\epsilon \sigma_x + \delta \sigma_z) + \frac{1}{2} \lambda_z \cos(\omega_0 t) \sigma_z. \quad (\text{A2})$$

In the qubit basis corresponding to the excited $|e\rangle$ and ground $|g\rangle$ states of the Hamiltonian in Eq. (A1), we can derive the longitudinal and the transverse couplings between the qubit and external field from Eq. (A2). However, if the qubit works at the optimal point with $\epsilon = 0$,

then the time dependent Hamiltonian in Eq. (A2) becomes into

$$H' = \frac{1}{2}\delta\sigma_z + \frac{1}{2}\lambda_z \cos(\omega_0 t)\sigma_z = \frac{1}{2}[\delta + \lambda_z \cos(\omega_0 t)]\sigma_z, \quad (\text{A3})$$

which has only longitudinal coupling. Here, we note that the coupling constant λ_z can be negative or positive by choosing the initial phase of the time-dependent external magnetic flux. This Hamiltonian can also be explained as that the qubit frequency is periodically modulated by the external field. This longitudinal coupling can result in the decoupling of the qubit from its environment.

Appendix B: Periodic Superconducting qubit chains

As shown in Fig. 10, there are four current loops in the gap-tunable flux qubit, thus different types of tunable couplings can be created via different loops. For example, the longitudinal coupling $\sigma_j^z \sigma_{j+1}^z$ between the j th and $(j+1)$ th qubits in the qubit chain can be realized by inductively coupling them through their α -loops [102]. However, in this paper, we mainly focus on the transverse coupling $\sigma_j^x \sigma_{j+1}^x$ between the qubits via ϵ -loops. Here, σ_j^x , σ_j^y , and σ_j^z denote Pauli operators, which are defined in the qubit basis $|g\rangle_j$ and $|e\rangle_j$ of the j th qubit.

To demonstrate different topological physics with gap-tunable flux qubits, in this section, we mainly show how to realize two coupling mechanism between gap-tunable flux qubits. (i) The qubits are directly coupled to each other via a mutual inductance, with fixed coupling strengths between qubits, but the frequencies of qubits can be either modulated or fixed. (ii) The qubits are indirectly coupled to each other via a coupler, thus both the qubit frequencies and the coupling strengths between qubits can be controlled. The first approach might be experimentally challenging, but the second one is more popular in recent experiments.

1. Qubit chain with fixed coupling strength

As schematically shown in Fig. 11, the qubits in the chain can be directly coupled to each other, that is, $2N$ identical gap-tunable flux qubits in the chain are directly coupled to each other through their mutual inductance via ϵ -loops. We assume that each qubit is only coupled to its nearest neighbors, the coupling strength between j th and $(j+1)$ th qubits can be obtained by $J = MI_{pj}I_{p(j+1)}$. Here M is the mutual inductance between the j th and $(j+1)$ th qubit loops, I_{pj} and $I_{p(j+1)}$ are the current circulating main loops of the j th and $(j+1)$ th qubits. Projecting J onto the eigenstates of the j th and $(j+1)$ th qubits, i.e., the states $|g\rangle_j$, $|g\rangle_{j+1}$, $|e\rangle_j$, and $|e\rangle_{j+1}$, we can obtain the coupled Hamiltonian, which includes the longitudinal coupling term $\sigma_j^z \sigma_{j+1}^z$ with the coefficient $g_{j,j+1}^z$, transverse coupling term $\sigma_j^x \sigma_{j+1}^x$ with the coefficient $g_{j,j+1}^x$, and cross coupling terms, e.g., $\sigma_j^x \sigma_{j+1}^z$ with

the coefficient $g_{j,j+1}^x$. Detailed analysis in the Appendix shows that the interaction via the main loops only results in transverse coupling when the qubits work at the optimal point, while the coefficients $g_{j,j+1}^z$ and $g_{j,j+1}^x$ of the longitudinal and cross couplings are zero.

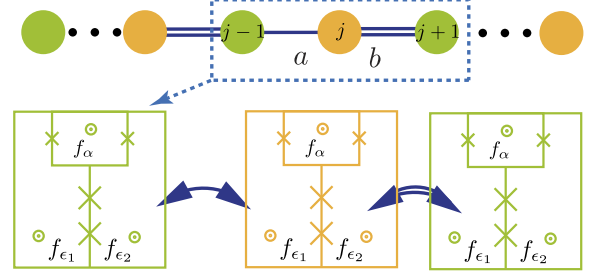


FIG. 11. Schematic diagram for the chain of coupled gap-tunable flux qubits with alternating coupling strengths a and b (Top panel). As shown in the lower panel, each qubit is coupled to its nearest-neighbors via the flux f_{ϵ_i} . The different coupling strengths a and b are created by varying the spacing between the qubits. The frequency of the qubit can be tuned in situ by the magnetic frustration f_α threading the α -loop.

To make the qubit have long coherence, we assume that all gap-tunable qubits in the chain work at the optimal point in the following discussions, then there is only transverse coupling between the qubits. As shown in the Appendix, the coupling coefficient $g_{j,j+1}^x$ of the transverse coupling between the j th and $(j+1)$ th qubits is written as $g_{j,j+1}^x = Mg_{\epsilon,\perp}^j g_{\epsilon,\perp}^{j+1}$, with $g_{\epsilon,\perp}^j = \langle e|I_{pj}|g\rangle_j$ and $g_{\epsilon,\perp}^{j+1} = \langle e|I_{p(j+1)}|g\rangle_{j+1}$. To create alternating coupling pattern as schematically shown in Fig. 10, the spacings between the qubits need to be varied respectively in order to alter M . This is experimentally accessible with current technology of the superconducting qubit circuits. The qubit chain is fabricated such that $a \equiv g_{(2m-1),2m}^x$ and $b \equiv g_{2m,(2m+1)}^x$ with $m = 1, 2, \dots, L$. We note that $b = 0$ when $m = L$. Then, the Hamiltonian of the coupled-qubit chain can be written as

$$H = \sum_{j=1}^{2N} \frac{\omega_j}{2} \sigma_j^z + \sum_{j \in \text{odd}}^{2N} a(\sigma_j^+ \sigma_{j+1}^- + \text{H.c.}) + \sum_{j \in \text{even}}^{2N} b(\sigma_j^+ \sigma_{j+1}^- + \text{H.c.}), \quad (\text{B1})$$

with ω_j denoting the frequency of the qubit. Because we assume that all qubits are identical, thus the qubits have the same frequency, that is, $\omega_j = \omega$ with $j = 1, \dots, 2N$. That is, the qubits resonantly interact with each other, and then we can make rotating wave approximation such that the transverse coupling term $\sigma_j^x \sigma_{j+1}^x$ between the j th and $(j+1)$ th qubits is approximated as $\sigma_j^x \sigma_{j+1}^x \approx (\sigma_j^+ \sigma_{j+1}^- + \sigma_j^- \sigma_{j+1}^+)$. It is clear that the coupling strengths a and b are fixed once the circuit is fabricated.

As shown in Fig. 11 and discussed in Section A, when the qubit works at the optimal point, the frequency mod-

ulation can be only done by applying the time-dependent magnetic flux through the α -loop. However, when all the qubits do not work at the optimal point, although the frequency of each qubit and the coupling strength between the qubits can be modulated by a time-dependent magnetic flux applied through the main loop of each qubit [59], the coherence of the qubits becomes worse. Thus, hereafter, we assume that the all qubits work at their optimal points. The qubit readout and control can be done in principle as in experiments [55–57]. In practise, there exists the next-nearest neighbor coupling in all superconducting circuits of many qubits with either capacitive or inductive coupling, these couplings can be minimized to be negligibly small by carefully designing circuits, e.g., as in the superconducting flux qubit chain with direct inductive coupling [56].

In above, we construct a qubit chain with fixed coupling. If the coupling between qubits in the chain can be tuned, then the system can be tuned from topological to non-topological phase, vice versa. In the natural atomic systems, the coupling is not tunable. However, the superconducting systems provide us ability to tune the coupling between the qubits. Below, we show two ways to tune the couplings between qubits in the chain.

2. Qubit chain with tunable couplings

In superconducting qubit circuits, the tunable coupling can be realized by using many methods. In this section, we show two methods, which are used for tunable coupling. One is that the qubit coupling can be tuned by modulating qubit frequencies with longitudinal coupling fields as shown in Eq. (A3). Another one is tunable coupling realized by adding the additional coupler between qubits.

a. tunable coupling realized by longitudinal coupling field

We now show how to tune the coupling by modulating the qubit frequencies. We assume that all flux qubits in the chain work at their optimal points, thus the qubit frequency can be modulated by applying the magnetic flux through the α -loop as shown in Refs. [103, 104]. In this case, the Hamiltonian $\omega_j \sigma_j^z / 2$ of the single qubit in Eq. (B1) is replaced by the modulated Hamiltonian in Eq. (A3), and the Hamiltonian in Eq. (B1) can be written as

$$H_M = \sum_{j=1}^{2N} \frac{\omega_j + u_j(t)}{2} \sigma_j^z + \sum_{j \in \text{odd}}^{2N} [a(\sigma_j^+ \sigma_{j+1}^- + \sigma_j^- \sigma_{j+1}^+)] + \sum_{j \in \text{even}}^{2N} [b(\sigma_j^+ \sigma_{j+1}^- + \sigma_j^- \sigma_{j+1}^+)]. \quad (\text{B2})$$

with $u_j(t) = \lambda_j \cos(\omega_{0j}t)$. Here, λ_j is proportional to the strength of the driving field and ω_{0j} is the frequency

of the driving field. For convenience, we also assume that the initial phases of all driving fields are zero. We now apply a unitary transformation $U(t) = \bigotimes U_j(t)$ to Eq. (B2) with [101].

$$U_j(t) = \exp \left[-\frac{i}{2} \left(\omega_j t + \frac{\lambda_j}{\omega_{0j}} \sin(\omega_{0j}t) \right) \sigma_j^z \right] \quad (\text{B3})$$

then we find that the term $u_j(t)$ in Eq. (B2) is canceled, and then operators σ_j^\pm become into

$$U_j^\dagger(t) \sigma_j^\pm U_j(t) = \sigma_j^\pm \exp \left[\pm i \left(\omega_j t + \frac{\lambda_j}{\omega_{0j}} \sin(\omega_{0j}t) \right) \right] = \sum_{n=-\infty}^{\infty} i^n \exp[\pm i(\omega_j + n\omega_{0j}t) J_n^j(\pm\alpha_j)] \quad (\text{B4})$$

with $\alpha_j \equiv \lambda_j / \omega_{0j}$ and the Bessel functions $J_n^j(\pm\alpha_j)$ of the first kind. Here, j is the index of the j th qubit.

If all the qubits are identical and the frequencies of the driving fields are the same, that is, $\omega_j = \omega$ and $\omega_{0j} = \omega_0$ with $j = 1, \dots, 2N$, then the Hamiltonian in Eq. (B2) becomes into an effective Hamiltonian

$$H_1 = \sum_{j \in \text{odd}}^{2N} [P \sigma_j^+ \sigma_{j+1}^- + \text{H.c.}] + \sum_{j \in \text{even}}^{2N} [Q \sigma_j^+ \sigma_{j+1}^- + \text{H.c.}]. \quad (\text{B5})$$

with effective coupling strengths

$$P = a \sum_{n=-\infty}^{\infty} (-1)^n J_n^j(\alpha_j) J_n^{(j+1)}(\alpha_{j+1}), \quad (\text{B6})$$

$$Q = b \sum_{n=-\infty}^{\infty} (-1)^n J_n^j(\alpha_j) J_n^{(j+1)}(\alpha_{j+1}), \quad (\text{B7})$$

after all oscillation terms of high frequencies are neglected. Here, j takes odd and even numbers for coefficients A and B , respectively. It is clear that the coefficients A and B can be tuned by changing ratios $\alpha_j \equiv \lambda_j / \omega_{0j}$ through the amplitudes of driving fields when the frequencies ω_{0j} are given.

However, in practise, the qubit frequencies are not exactly same, this provides us more convenient way to tune the coupling strength via frequency matching [59]. If we assume that $\omega_j - \omega_{j-1} = \omega_{0j}$ for odd number j and $\omega_j - \omega_{j-1} = \omega_{0(j-1)}$ for even number, then the effective Hamiltonian can be written as

$$H_2 = \sum_{j \in \text{odd}}^{2N} [A' \sigma_j^+ \sigma_{j+1}^- + \text{H.c.}] + \sum_{j \in \text{even}}^{2N} [B' \sigma_j^+ \sigma_{j+1}^- + \text{H.c.}]. \quad (\text{B8})$$

with effective coupling strengths

$$P = ia J_0^j(\alpha_j) J_1^{(j+1)}(\alpha_{j+1}), \quad (\text{B9})$$

$$Q = ib J_1^j(\alpha_j) J_0^{(j+1)}(\alpha_{j+1}), \quad (\text{B10})$$

which has been experimentally demonstrated in a qubit chain with five transmon qubits [105] and also two coupled qubits [104]. Therefore, tunable couplings between qubits can be realized by modulating the qubit frequencies without increasing the complexity of the circuit.

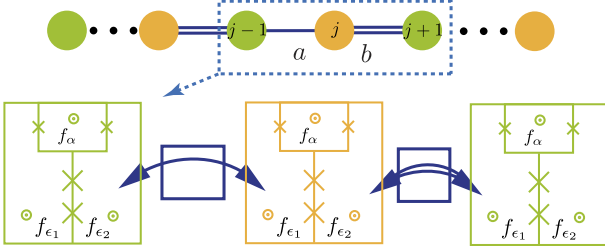


FIG. 12. Couplers (rectangle) are inserted between qubits in the chain to achieve time-dependent tunable coupling strengths. The couplers can be superconducting quantum interference devices, superconducting qubits, LC circuits, or other superconducting elements.

b. tunable coupling via couplers

If the qubits work at the optimal point and their frequencies are not modulated, then as schematically shown in Fig. 12, additional couplers [59–64] can be used to achieve tunable couplings between the qubits. Various couplers have been demonstrated in the two-qubit cases [59–70] and can be extended to large scale of qubit circuits. In this case, using the same procedure for the directly coupled qubit chain in Fig. 11, we can write out the full Hamiltonian of the qubit chain, in which each pair of qubit is indirectly coupled through their coupler. The effective couplings between qubits can be obtained after the variables of the couplers are eliminated.

The coupler can work at either classical or quantum regime. When the couplers work at the classical regime, the variables of the couplers can be adiabatically eliminated as discussed in Ref. [61]. When the couplers work at the quantum regime, we usually assume that the transition frequency from the ground to first excited state of the coupler is much larger than the qubit frequencies. Then we can eliminate the variables of the couplers by the large detuning approximation [106]. In either way, we can obtain an effective Hamiltonian as

$$\begin{aligned}
 H_C = & \sum_{j \in \text{odd}}^{2N} \left[\frac{\omega'_j}{2} \sigma_j^z + a(t) (\sigma_j^+ \sigma_{j+1}^- + \sigma_j^- \sigma_{j+1}^+) \right] \\
 & + \sum_{j \in \text{even}}^{2N} \left[\frac{\omega'_j}{2} \sigma_j^z + b(t) (\sigma_j^+ \sigma_{j+1}^- + \sigma_j^- \sigma_{j+1}^+) \right],
 \end{aligned} \tag{B11}$$

which has the same form as in Eq. (B1). However, here the parameters $a(t)$ and $b(t)$ are time-dependent..

There are differences between Eq. (B1) and Eq. (B11). The bare qubit frequency ω in Eq. (B1) is modified to ω'_j in Eq. (B11) when the couplers are eliminated. The effective coupling strengths between qubits induced by couplers are tunable now and can be denoted by time-dependent parameters $a(t)$ and $b(t)$. The tunable coupling strengths between qubits are realized by individually applying the magnetic flux through the loop of each coupler. For the coupler which works in the quantum regime, the applied magnetic flux changes the frequency of the coupler such that the detuning between qubits and coupler is changed, and then the effective coupling between qubits is changed with the change of applied magnetic flux. For the coupler which works in the classical regime, the magnetic flux changes the effective mutual inductance between the qubits, and then the coupling strength is changed. Therefore, in both the cases, we can consider that the effective coupling strengths are time-dependent.

Here we further note that if the qubit frequency is also modulated for the qubit with the coupler, then we can obtain an effective Hamiltonian with both the tunable coupling and qubit frequency modulation. Such full controlled circuit enables us to demonstrate various one-dimensional topological model.

Appendix C: Topologically protected solitons

We now study how the proposed superconducting qubit chain with Hamiltonian in Eq. (B1) can be used to demonstrate topologically protected solitons when there is only a single-excitation in $2N$ superconducting qubits. To clearly illustrate this, let us fix the coupling strength between the even qubit and its right neighbor, e.g., hereafter we take the coupling strength b as a unit, i.e., $b = 1$. Then we study how the hopping amplitude a , the hopping strength between the odd qubit and its right neighbor, affects the energy spectrum and the topological properties of the chain.

In our simulation, for concreteness, the total number of superconducting qubits is set as $2N = 14$. We plot, in Fig. 13(a), the energy spectrum of the Hamiltonian in Eq. (3) and corresponding eigenfunctions $|\psi_l\rangle$ where $l = 1, \dots, 2N$ in the basis $|e_j\rangle$ shown in Eq. (2). They are plotted in Figs. 13(b) and (c) with $a = 0.1$, in Fig. 13(d) with $a = 1$. Here, emphasize that the tunable coupling strengths a and b can be realized via frequency modulation or couplers as shown in above studies..

Figure 13 bears several interesting features. (i) Due to the bipartite lattice structure, the spectrum exhibits two band. (ii) The spectrum is symmetric around zero. For any state with energy E , there is a partner with energy $-E$. This stems from the chiral symmetry of the SSH model [10]. (iii) For the $E \neq 0$ states, *all* the wave functions have support on both even and odd qubits, also known as the bulk states. Figure 13(d) shows a typical bulk state wave function corresponding to the point $a =$

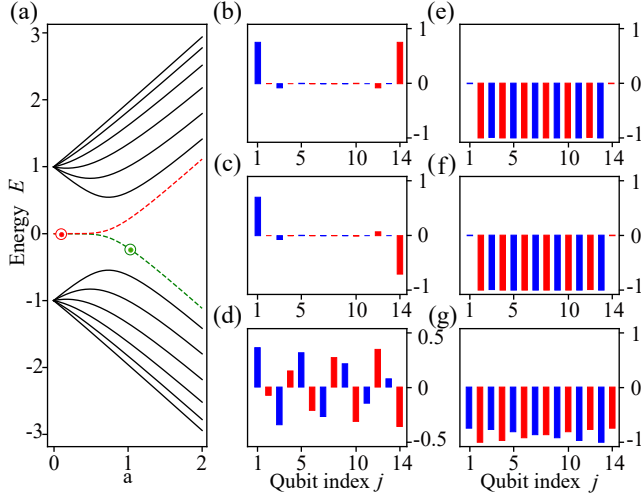


FIG. 13. Spectrum and wave functions of the Hamiltonian (3). The total number of qubits is assume as 14. (a) Energy spectrum verses the coupling strength a with $b = 1$. Degenerate wave functions, corresponding to the zero-energy mode with $a = 0.1$ indicated by a red point in (a), are shown in (b) and (c), respectively. A typical bulk state at the point $a = 1$, marked by a green point in (a), is plotted in (d). The observables $\langle \sigma_n^z \rangle$ of the corresponding wave functions in (b), (c) and (d), are shown in (e), (f) and (g). All the navy blocks denote the amplitude on the odd qubits, while the red blocks represent the even sites.

$b = 1$ marked by a red point in Fig. 13 (a). (iii) There is a zero energy ($E = 0$) mode lying in the middle of the bulk gap, where $a < b$. The zero-energy mode has two degenerate states. They are presented in Fig. 13 (b) and (c) corresponding to $a = 0.1$ point marked by a star in Fig. 13 (a). The eigenfunctions are localized at the left and right edge, and decay exponentially towards the bulk.

The appearance of $E = 0$ mode with localized eigenfunctions is the key feature of the topological phase when $a < b$. The localized eigenfunctions shown in Figs.13(b) and (c) are the superpositions $|L\rangle \pm |R\rangle$ of the left and right edge states $|L\rangle$ and $|R\rangle$. Here the left edge state is defined as

$$|L\rangle = \sum_{j \in \text{odd}} a_j |e_j\rangle, \quad (\text{C1})$$

where j is an odd number and a_j is the amplitude on the odd qubits. Similarly, the right edge state is written as

$$|R\rangle = \sum_{j \in \text{even}} b_j |e_j\rangle, \quad (\text{C2})$$

here j is an even number and b_m is the amplitude on the even qubits. Note the vanishing amplitudes on the even (odd) site of the left (right) edge state are the consequence of the chiral symmetry. The decay depth into

the bulk is characterized by [10]

$$|a_j| = |a_1| \exp\left(-\frac{j-1}{2\xi}\right), \quad (\text{C3})$$

where the localization length $\xi = (\ln|b| - \ln|a|)^{-1}$. When the ratio $|b|/|a|$ becomes appreciably large, the wave function will almost be confined at the first and last qubit.

The particle distributions in the eigenfunctions $|\psi_l\rangle$ of the qubit chain can be measured via the variable σ_n^z of each qubit, with the measurement result $\langle \psi_l | \sigma_n^z | \psi_l \rangle$. Here, the subscript n denotes the n th qubit. We note that the in the single-excitation subspace, the Pauli operator σ_n^z can be expressed as $\sigma_n^z = 2|e_n\rangle\langle e_n| - I$, where I is the identity matrix. Although the qubits are coupled to each other, the excitation stays at the end of qubit chain as shown in Fig. 13 (e) and (f).

To demonstrate the existence of edge states, we study the quench dynamics after the first qubit is flipped. That is, let us assume that all the qubits are initially in the spin-down state, then a π pulse is applied to flip the first qubit. The dynamics of the qubit chain can be measured by

$$\langle \sigma_n^z(t) \rangle = \langle e_1 | e^{iHst} \sigma_n^z e^{-iHst} | e_1 \rangle. \quad (\text{C4})$$

with the Hamiltonian given in Eq. (3). Below, we compare the dynamics of a topological SSH chain, described by the Hamiltonian in Eq. (3) when $a = 0.1$ and $b = 1$, with a transverse spin chain, described by the Hamiltonian in Eq. (3) when $a = b = 1$.

To model the small divergence of the qubits resulted from the sample fabrication, a random noise η is introduced to the coupling strengths a and b , as well as the frequency ω in Eq. (3). Here η follows Gaussian distribution with mean value 0, and a standard deviation 0.01. That is the fluctuations of the coupling strength and qubit frequencies are 10% of the smaller coupling strength a .

For the topological SSH chain with $a = 0.1$ and $b = 1$ in the Hamiltonian of Eq. (3), Fig. 14(a) and (b) show that the excitation remains as a soliton at the first qubit. This can be understood by the evolution of the wave function

$$|\psi(t)\rangle = \sum_l e^{-E_l t/\hbar} \langle \psi_l | e_1 \rangle |\psi_l\rangle, \quad (\text{C5})$$

where $|\psi_l\rangle$ denotes the l th eigenfunctions of the Hamiltonian in Eq. (3) with corresponding eigenenergy E_l . We start with the state $|e_1\rangle$ after the excitation is injected at the first qubit. $|e_1\rangle$ has a substantial overlap with the degenerate edge states with corresponding eigenenergy $E = 0$. This leads to a stationary state. Conversely, if we inject the excitation in the transverse Ising chain described by the Hamiltonian of Eq. (3) with $a = b = 1$, without localized edge states, it will quickly diffuse into the bulk. This can be seen from Figs. 14(c) and (d). The excitation at the first qubit quickly expands into the bulk, reaches the end of the qubit chain, and then is reflected back. The similar propagation of such excitations is demonstrated in Refs. [51, 52].

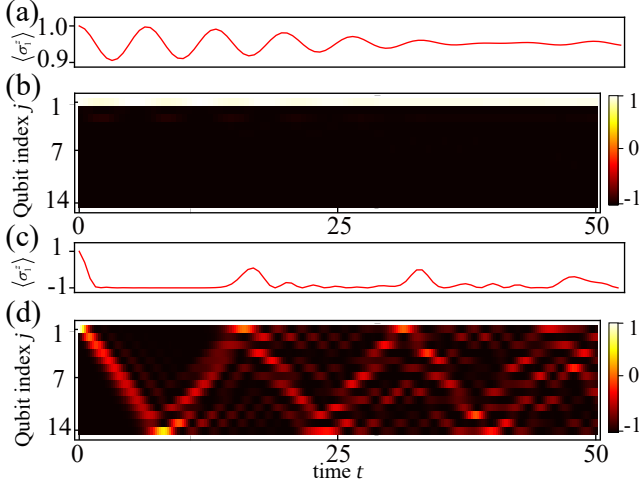


FIG. 14. Time evolution of $\langle \sigma_j^z \rangle$, after the first qubit is flipped to the spin-up state. (a) and (c) show the time evolution $\langle \sigma_1^z \rangle$ of the first qubit. (b) and (d) show the time evolution $\langle \sigma_j^z \rangle$ of all the qubits. A random noise with an amplitude of 10% of the coupling strength a is added to the qubit frequency and coupling strength. The topological SSH chain with $a = 0.1$ and $b = 1$ is shown in (a) and (b). The transverse Ising chain with $a = b = 1$ is plotted in (c) and (d). In our plot, the qubit number in the chain is assumed as 14.

In summary, due to the alternating coupling pattern $a < b$ of the whole chain, the soliton is topologically protected and robust against disorder. This is because the soliton resides in the gap, extra energy is required if we want to excite the soliton to other states. We have also shown the random noise added to the parameters in Eq. (B1) have no appreciable influence on the soliton state.

Though the soliton appears at the very end of the chain, it can also be created at the interface between the topological phase with $a < b$ and topologically trivial phase with $a > b$. For example, as shown in Ref. [107], if a defect is created at the center of a topological SSH chain, then a zero energy mode localizes at the defect. Moreover, the defect can serve as a high-fidelity memory, which is topologically protected. An arbitrary state encoded with the presence and absence of the localized state can allow for perfect state transfer in the spin chain [107, 108].

Appendix D: Hamiltonian derivation of the gap-tunable flux qubit

In this section, the Hamiltonian of inductively coupled gap-tunable flux qubit (Fig. 10) will be derived. With our design, the qubit frequencies and the couplings between qubits (e.g. in Eq. (B1)) can be tailored and tuned in situ by external fluxes.

1. Hamiltonian of single qubit

A Gap-tunable flux qubit [55–57], as shown in Fig. 15, replaces the α junction of a three-junction flux qubit [71] with a SQUID. This introduces an external controllable flux f_α to tune α in situ, thus changing the gap (qubit frequency). To keep f_α from affecting the biasing flux f_ϵ threading the main loop, a gradiometric design is adopted. In this 8-shaped design, the central current of the three-junction flux qubit is split into two opposite running currents. Because the magnetic flux generated by these two currents now cancel each other in the main loop, independent control over both flux f_α and f_ϵ is ensured. Different types of tunable couplings can also be created via different loops. For example, longitudinal coupling between two qubits ($\sigma_i^z \sigma_{i+1}^z$) can be realized by inductively coupling two qubits through their f_α -loop [102]. In this paper, we focus on the transverse coupling ($\sigma_i^x \sigma_{i+1}^x$) through the f_ϵ -loop.

We follow the notations in Refs. [56, 102], as shown in Fig. 15. We assume the phase accumulated along the main trap-loop is θ . Here β denotes the ratio between the circumference of the α -loop to the main trap-loop. The magnetic frustration threading the corresponding loop is denoted by f_i . The phase difference across the junction is φ_i .

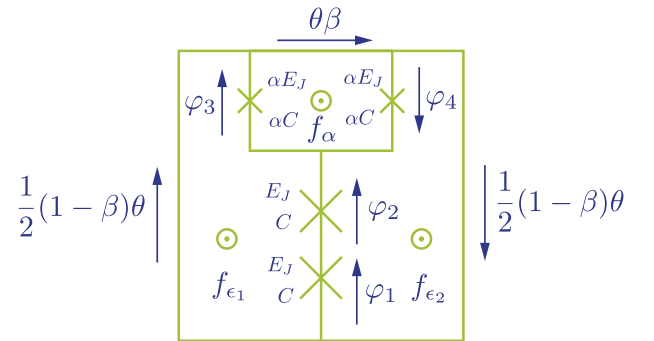


FIG. 15. Circuit representation of a gap tunable flux qubit. The sign \times denotes the Josephson junction. The long arrows denote the current direction. The phase accumulated along the main trap-loop is denoted by θ . The parameter β denotes the ratio between the circumference of the α -loop and that of the main trap-loop. The $f_\alpha = \Phi_\alpha / \Phi_0$ denotes the reduced magnetic flux threading the α loop, and $f_1 = \Phi_1 / \Phi_0$ and $f_2 = \Phi_2 / \Phi_0$ denote the reduced magnetic fluxes through the left and right parts of the main loop, respectively. E_J and C_J denote the Josephson energy and capacitance, respectively. The phase difference across each junction is denoted by φ_i .

Then the flux quantization conditions for the main

trap-loop, α -loop, f_{ϵ_1} -loop, f_{ϵ_2} -loop are

$$\begin{aligned} \theta + 2\pi(f_{\epsilon_1} + f_{\epsilon_2} + f_\alpha) &= 2\pi N \\ \varphi_3 + \varphi_4 + \beta\theta + 2\pi f_\alpha &= 2\pi N_\alpha \\ \frac{1}{2}(1 - \beta)\theta - \varphi_3 - \varphi_2 - \varphi_1 + 2\pi f_{\epsilon_1} &= 2\pi N_1 \\ \frac{1}{2}(1 - \beta)\theta + \varphi_1 + \varphi_2 - \varphi_4 + 2\pi f_{\epsilon_2} &= 2\pi N_2, \end{aligned} \quad (\text{D1})$$

where N_i is the number of trapped fluxoids.

Using above conditions, φ_3 , φ_4 can be expressed in terms of φ_1 , φ_2 ,

$$\begin{aligned} \varphi_3 &= -\pi[\beta(N - f_\Sigma) + f_\alpha] - (\varphi_1 + \varphi_2) - \pi(n - f_\epsilon) + \pi N_\alpha, \\ \varphi_4 &= -\pi[\beta(N - f_\Sigma) + f_\alpha] + (\varphi_1 + \varphi_2) + \pi(n - f_\epsilon) + \pi N_\alpha, \end{aligned}$$

where $f_\Sigma = f_{\epsilon_1} + f_{\epsilon_2} + f_\alpha$, $f_\epsilon = f_{\epsilon_1} - f_{\epsilon_2}$, $N = N_1 + N_2 + N_\alpha$, $n = N_1 - N_2$. For simplicity, we assume $N_\alpha = 0$ in the following analysis.

Following the standard circuit quantization process [109, 110], the charging energy of the capacitor represents the kinetic energy, while the Josephson energy represents the potential energy. Then the Lagrangian of the circuit in terms of φ_1 , φ_2 is

$$\begin{aligned} \mathcal{L}(\dot{\varphi}_i, \varphi) &= \\ & \left(\frac{\hbar}{2e}\right)^2 [(1 + 2\alpha)\frac{C}{2}(\dot{\varphi}_1^2 + \dot{\varphi}_2^2) + 2\alpha C\dot{\varphi}_1\dot{\varphi}_2] \\ & - E_J [2(1 + \alpha) - \cos\varphi_1 - \cos\varphi_2 - \\ & 2\alpha \cos\{\pi[\beta(N - f_\Sigma) + f_\alpha]\} \cos[(\varphi_1 + \varphi_2) + \pi(n - f_\epsilon)]]. \end{aligned} \quad (\text{D3})$$

The canonical momentum p_i conjugated to coordinate φ_i is

$$\begin{aligned} p_1 &= \frac{\partial L}{\partial \dot{\varphi}_1} = \left(\frac{\hbar}{2e}\right)^2 [(1 + 2\alpha)C\dot{\varphi}_1 + 2\alpha C\dot{\varphi}_2], \\ p_2 &= \frac{\partial L}{\partial \dot{\varphi}_2} = \left(\frac{\hbar}{2e}\right)^2 [(1 + 2\alpha)C\dot{\varphi}_2 + 2\alpha C\dot{\varphi}_1]. \end{aligned} \quad (\text{D4})$$

The Hamiltonian is related to the Lagrangian by Legendre transformation

$$\begin{aligned} H(p_i, \varphi_i) &= \sum p_i \dot{\varphi}_i - \mathcal{L} \\ &= \frac{4E_C}{(1 + 4\alpha)} [(1 + 2\alpha)n_1^2 - 4\alpha n_1 n_2 + (1 + 2\alpha)n_2^2] \\ & + E_J [2(1 + \alpha) - \cos\varphi_1 - \cos\varphi_2 \\ & - 2\alpha \cos\{\pi[\beta(N - f_\Sigma) + f_\alpha]\} \cos[(\varphi_1 + \varphi_2) + \pi(n - f_\epsilon)]], \end{aligned} \quad (\text{D5})$$

where charging energy of the junction is defined as $E_C = e^2/2C$. We also introduced the number operator of Cooper-pairs on the junction capacitor $n_i = p_i/\hbar$, which can also be written as $n_i = -i\partial/\partial\varphi_i$.

The energy levels of the qubit are solved numerically by the plane-wave solutions $\Psi(\varphi_1, \varphi_2) =$

$\frac{1}{2\pi} \sum_{k,l=-N}^N c_{k,l} \exp\{-i(k\varphi_1 + l\varphi_2)\}$. Here k (l) is an integer, corresponding to a state that has k (l) Cooper pairs on junction 1 (2). The total charge states is set to $N = 15$.

The energy levels as a function of the bias flux f_ϵ are plot in Fig. 16 (a). At the optimal working point where $f_\epsilon = 0$, the lowest two energy levels is well separated from higher excited states. The splitting of these two levels is the qubit frequency ω . As shown in Fig. 16 (b), ω can be tuned by f_α .

2. Qubit-qubit coupling

(D2) As shown in Fig. 10, the qubits are coupled inductively via f_ϵ -loop. The current $I_{p,j+1}$ circulating the f_ϵ loop of the $j + 1$ th qubit can induce a change of flux δf_j in the f_ϵ loop of qubit j , giving rise to the coupling term $J = MI_{pj}I_{p(j+1)}$, where the current $I_{pj} = \partial\mathcal{H}_j/\partial f_\epsilon$. Here we assume δf_j does not affect f_α -loop.

As shown in the main text, the transverse coupling strength $a = g_{\epsilon,\pm}^j g_{\epsilon,\pm}^{j+1}$, with

$$g_{\epsilon,\pm} = \langle e | \frac{\partial\mathcal{H}}{\partial f_\epsilon} | g \rangle. \quad (\text{D7})$$

For simplicity we have dropped the superscript j .

Similarly the longitudinal coupling $\lambda\sigma_j^z\sigma_{j+1}^z$ is also possible, where $\lambda = g_{\epsilon,\parallel}^j g_{\epsilon,\parallel}^{j+1}$, with

$$g_{\epsilon,\parallel} = \langle + | \frac{\partial\mathcal{H}}{\partial f_\epsilon} | - \rangle. \quad (\text{D8})$$

Here $|\pm\rangle = (|e\rangle \pm |g\rangle)/\sqrt{2}$.

Note because of the gradiometric geometry, the flux in the main trap loop is insensitive to a homogeneous magnetic field. Thus only the asymmetrical flux $f_\epsilon = f_{\epsilon_1} - f_{\epsilon_2}$ contributes in the coupling.

We plot $g_{\epsilon,\parallel}$ and $g_{\epsilon,\pm}$ as a function of the bias flux f_ϵ in Fig. 16 (c) and (d). At the optimal working point $f_\epsilon = 0$, $g_{\epsilon,\pm}$ is the largest, while $g_{\epsilon,\parallel} = 0$. This is consistent with the symmetry of the flux qubit. The potential energy is symmetrical about the optimal working point, the loop currents in the ground state $I_0 = \langle g | \frac{\partial\mathcal{H}}{\partial f_\epsilon} | g \rangle$, and in the first excited $I_1 = \langle e | \frac{\partial\mathcal{H}}{\partial f_\epsilon} | e \rangle$ are zero. Thus when biasing at the optimal point, the qubit is first-order insensitive to dephasing noise.

To summarize, when the qubits are all biased at the optimal working point, only transverse coupling are present. Even there is a residual longitudinal coupling, this will only add fluctuations to the diagonal term of the matrix in the single-spin excitation subspace. However, the previous result shows the chain is robust under fluctuations. To create alternating coupling pattern of the SSH model, one can vary the qubit spacing, that will change the mutual inductance M .

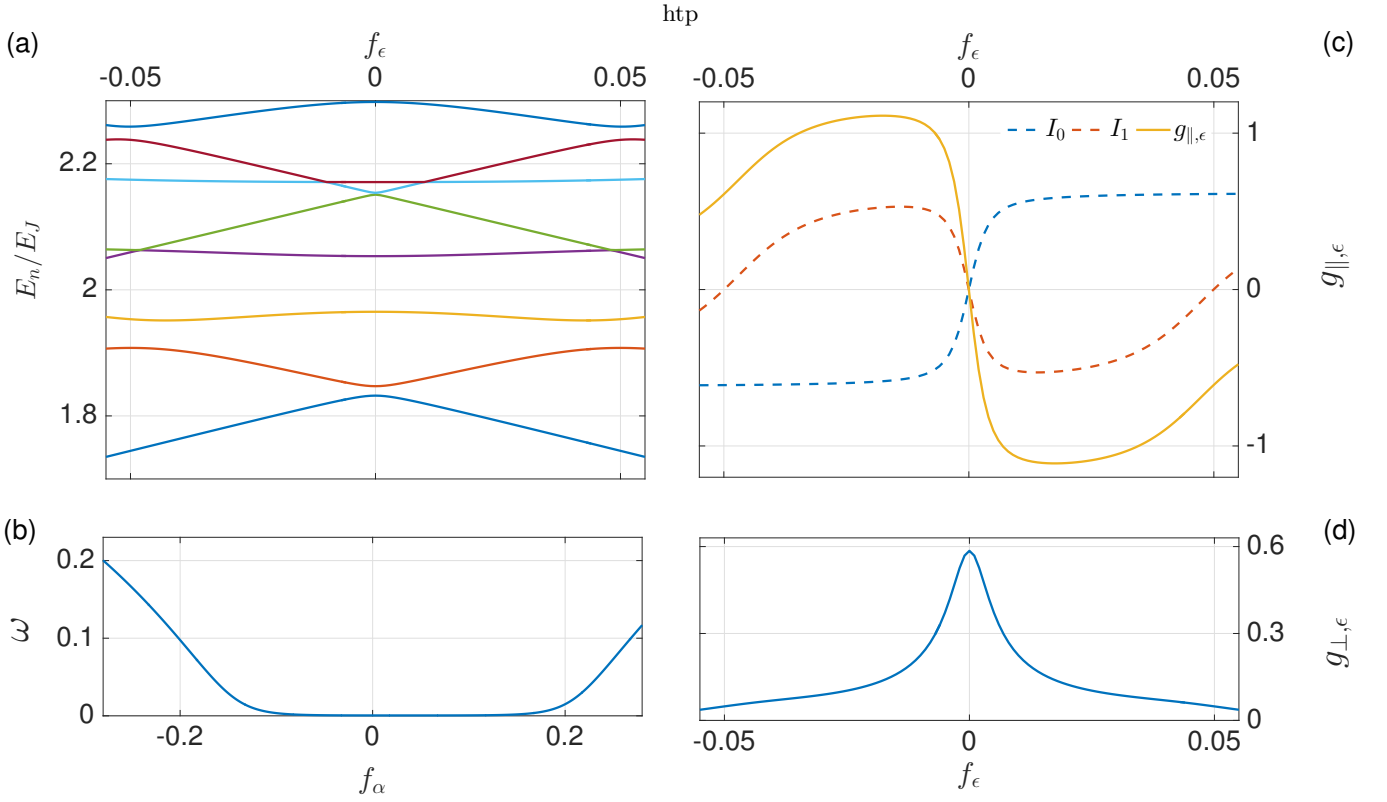


FIG. 16. (a) Dependence of energy levels on the frustration f_ϵ , with $f_\alpha = 0.2$. (b) The energy gap ω as a function of f_α when biased at the optimal working point $f_\epsilon = 0$. (c) Longitudinal coupling strength through f_ϵ loop, with $f_\alpha = 0.2$. (d) Transverse coupling strength through f_ϵ loop, with $f_\alpha = 0.2$. The rest parameters are $E_J = 1$, $E_J/E_C = 50$, $\alpha = 0.5$, $f_\Sigma = 50f_\alpha$, $\beta = 0.05$, $N = 1$, $n = 1$.

-
- [1] M. Z. Hasan and C. L. Kane, Colloquium : Topological insulators, *Rev. Mod. Phys.* **82**, 3045 (2010).
- [2] A. Stern and N. H. Lindner, Topological Quantum Computation—From Basic Concepts to First Experiments, *Science* **339**, 1179 (2013).
- [3] L. Lu, J. D. Joannopoulos, and M. Soljačić, Topological photonics, *Nat. Photonics* **8**, 821 (2014).
- [4] C.-C. Chien, S. Peotta, and M. Di Ventra, Quantum transport in ultracold atoms, *Nat. Phys.* **11**, 998 (2015).
- [5] N. Goldman, J. C. Budich, and P. Zoller, Topological quantum matter with ultracold gases in optical lattices, *Nat. Phys.* **12**, 639 (2016).
- [6] I. M. Georgescu, S. Ashhab, and F. Nori, Quantum simulation, *Rev. Mod. Phys.* **86**, 153 (2014).
- [7] W. P. Su, J. R. Schrieffer, and A. J. Heeger, Solitons in Polyacetylene, *Phys. Rev. Lett.* **42**, 1698 (1979).
- [8] W. P. Su, J. R. Schrieffer, and A. J. Heeger, Soliton excitations in polyacetylene, *Phys. Rev. B* **22**, 2099 (1980).
- [9] A. J. Heeger, S. Kivelson, J. R. Schrieffer, and W. P. Su, Solitons in conducting polymers, *Rev. Mod. Phys.* **60**, 781 (1988).
- [10] J. K. Asbóth, L. Oroszlány, and A. Pályi, *A Short Course on Topological Insulators*, Lecture Notes in Physics, Vol. 919 (Springer International Publishing, Cham, 2016).
- [11] H. Takayama, Y. R. Lin-Liu, and K. Maki, Continuum model for solitons in polyacetylene, *Phys. Rev. B* **21**, 2388 (1980).
- [12] R. Jackiw and C. Rebbi, Solitons with fermion number 1/2, *Phys. Rev. D* **13**, 3398 (1976).
- [13] J. Ruostekoski, G. V. Dunne, and J. Javanainen, Particle Number Fractionalization of an Atomic Fermi-Dirac Gas in an Optical Lattice, *Phys. Rev. Lett.* **88**, 180401 (2002).
- [14] L. Li, Z. Xu, and S. Chen, Topological phases of generalized Su-Schrieffer-Heeger models, *Phys. Rev. B* **89**, 085111 (2014).
- [15] C. Poli, M. Bellec, U. Kuhl, F. Mortessagne, and H. Schomerus, Selective enhancement of topologically induced interface states in a dielectric resonator chain, *Nat. Commun.* **6**, 6710 (2015).
- [16] T. Kitagawa, M. A. Broome, A. Fedrizzi, M. S. Rudner, E. Berg, I. Kassal, A. Aspuru-Guzik, E. Demler, and A. G. White, Observation of topologically protected bound states in photonic quantum walks, *Nat. Commun.* **3**, 882 (2012).
- [17] F. Cardano, A. D’Errico, A. Dauphin, M. Maffei, B. Piccirillo, C. de Lisio, G. De Filippis, V. Cataudella, E. Santamato, L. Marrucci, M. Lewenstein, and P. Massignan, Detection of Zak phases and topological

- invariants in a chiral quantum walk of twisted photons, *Nat. Commun.* **8**, 15516 (2017).
- [18] M. Atala, M. Aidelsburger, J. T. Barreiro, D. Abanin, T. Kitagawa, E. Demler, and I. Bloch, Direct measurement of the Zak phase in topological Bloch bands, *Nat. Phys.* **9**, 795 (2013).
- [19] E. J. Meier, F. A. An, and B. Gadway, Observation of the topological soliton state in the Su-Schrieffer-Heeger model, *Nat. Commun.* **7**, 13986 (2016).
- [20] M. Lohse, C. Schweizer, O. Zilberberg, M. Aidelsburger, and I. Bloch, A Thouless quantum pump with ultracold bosonic atoms in an optical superlattice, *Nat. Phys.* **12**, 350 (2015).
- [21] S. Nakajima, T. Tomita, S. Taie, T. Ichinose, H. Ozawa, L. Wang, M. Troyer, and Y. Takahashi, Topological Thouless pumping of ultracold fermions, *Nat. Phys.* **12**, 296 (2016).
- [22] J. Zak, Berry's phase for energy bands in solids, *Phys. Rev. Lett.* **62**, 2747 (1989).
- [23] D. J. Thouless, Quantization of particle transport, *Phys. Rev. B* **27**, 6083 (1983).
- [24] J. Q. You and F. Nori, Atomic physics and quantum optics using superconducting circuits, *Nature* **474**, 589 (2011).
- [25] M. H. Devoret and R. J. Schoelkopf, Superconducting Circuits for Quantum Information: An Outlook, *Science* **339**, 1169 (2013).
- [26] X. Gu, A. F. Kockum, A. Miranowicz, Y.-X. Liu, and F. Nori, Microwave photonics with superconducting quantum circuits, *Phys. Rep.* **718-719**, 1 (2017).
- [27] V. Gritsev and A. Polkovnikov, Dynamical quantum Hall effect in the parameter space, *Proc. Natl. Acad. Sci.* **109**, 6457 (2012).
- [28] P. J. Leek, J. M. Fink, A. Blais, R. Bianchetti, M. Goppl, J. M. Gambetta, D. I. Schuster, L. Frunzio, R. J. Schoelkopf, and A. Wallraff, Observation of Berry's Phase in a Solid-State Qubit, *Science* **318**, 1889 (2007).
- [29] S. Berger, M. Pechal, S. Pugnetti, A. A. Abdumalikov, L. Steffen, A. Fedorov, A. Wallraff, and S. Filipp, Geometric phases in superconducting qubits beyond the two-level approximation, *Phys. Rev. B* **85**, 220502 (2012).
- [30] S. Berger, M. Pechal, A. A. Abdumalikov, C. Eichler, L. Steffen, A. Fedorov, A. Wallraff, and S. Filipp, Exploring the effect of noise on the Berry phase, *Phys. Rev. A* **87**, 060303 (2013).
- [31] M. D. Schroer, M. H. Kolodrubetz, W. F. Kindel, M. Sandberg, J. Gao, M. R. Vissers, D. P. Pappas, A. Polkovnikov, and K. W. Lehnert, Measuring a Topological Transition in an Artificial Spin-1/2 System, *Phys. Rev. Lett.* **113**, 050402 (2014).
- [32] Z. Zhang, T. Wang, L. Xiang, J. Yao, J. Wu, and Y. Yin, Measuring the Berry phase in a superconducting phase qubit by a shortcut to adiabaticity, *Phys. Rev. A* **95**, 042345 (2017).
- [33] P. Roushan, C. Neill, Y. Chen, M. Kolodrubetz, C. Quintana, N. Leung, M. Fang, R. Barends, B. Campbell, Z. Chen, B. Chiaro, A. Dunsworth, E. Jeffrey, J. Kelly, A. Megrant, J. Y. Mutus, P. J. J. O'Malley, D. Sank, A. Vainsencher, J. Wenner, T. White, A. Polkovnikov, A. N. Cleland, and J. M. Martinis, Observation of topological transitions in interacting quantum circuits, *Nature* **515**, 241 (2014).
- [34] E. Flurin, V. V. Ramasesh, S. Hacohe-Gourgy, L. S. Martin, N. Y. Yao, and I. Siddiqi, Observing Topological Invariants Using Quantum Walks in Superconducting Circuits, *Phys. Rev. X* **7**, 031023 (2017).
- [35] V. V. Ramasesh, E. Flurin, M. Rudner, I. Siddiqi, and N. Y. Yao, Direct Probe of Topological Invariants Using Bloch Oscillating Quantum Walks, *Phys. Rev. Lett.* **118**, 130501 (2017).
- [36] X. Tan, Y. Zhao, Q. Liu, G. Xue, H. Yu, Z. Wang, and Y. Yu, Realizing and manipulating space-time inversion symmetric topological semimetal bands with superconducting quantum circuits, *npj Quantum Materials* **2**, 1 (2017).
- [37] X. Tan, D.-w. Zhang, Q. Liu, G. Xue, H.-F. Yu, Y.-Q. Zhu, H. Yan, S.-l. Zhu, and Y. Yu, Topological Maxwell Metal Bands in a Superconducting Qutrit, *Phys. Rev. Lett.* **120**, 130503 (2018).
- [38] Y. P. Zhong, D. Xu, P. Wang, C. Song, Q. J. Guo, W. X. Liu, K. Xu, B. X. Xia, C.-Y. Lu, S. Han, J.-W. Pan, and H. Wang, Emulating Anyonic Fractional Statistical Behavior in a Superconducting Quantum Circuit, *Phys. Rev. Lett.* **117**, 110501 (2016).
- [39] P. Roushan, C. Neill, A. Megrant, Y. Chen, R. Babbush, R. Barends, B. Campbell, Z. Chen, B. Chiaro, A. Dunsworth, A. G. Fowler, E. Jeffrey, J. Kelly, E. Lucero, J. Y. Mutus, P. J. J. O'Malley, M. Neeley, C. Quintana, D. Sank, A. Vainsencher, J. Wenner, T. White, E. Kapit, H. Neven, and J. Martinis, Chiral ground-state currents of interacting photons in a synthetic magnetic field, *Nat. Phys.* **13**, 146 (2016).
- [40] J. Koch, A. A. Houck, K. L. Hur, and S. M. Girvin, Time-reversal-symmetry breaking in circuit-QED-based photon lattices, *Phys. Rev. A* **82**, 043811 (2010).
- [41] A. Nunnenkamp, J. Koch, and S. M. Girvin, Synthetic gauge fields and homodyne transmission in Jaynes-Cummings lattices, *New J. Phys.* **13**, 095008 (2011).
- [42] F. Mei, J.-B. You, W. Nie, R. Fazio, S.-L. Zhu, and L. C. Kwek, Simulation and detection of photonic Chern insulators in a one-dimensional circuit-QED lattice, *Phys. Rev. A* **92**, 041805 (2015).
- [43] F. Mei, Z.-y. Xue, D.-w. Zhang, L. Tian, C. Lee, and S.-l. Zhu, Witnessing topological Weyl semimetal phase in a minimal circuit-QED lattice, *Quantum Sci. Technol.* **1**, 015006 (2016).
- [44] Z.-H. Yang, Y.-P. Wang, Z.-Y. Xue, W.-L. Yang, Y. Hu, J.-H. Gao, and Y. Wu, Circuit quantum electrodynamics simulator of flat band physics in a Lieb lattice, *Phys. Rev. A* **93**, 062319 (2016).
- [45] J. Tangpanitanon, V. M. Bastidas, S. Al-Assam, P. Roushan, D. Jaksch, and D. G. Angelakis, Topological Pumping of Photons in Nonlinear Resonator Arrays, *Phys. Rev. Lett.* **117**, 213603 (2016).
- [46] M. Sameti, A. Potočnik, D. E. Browne, A. Wallraff, and M. J. Hartmann, Superconducting quantum simulator for topological order and the toric code, *Phys. Rev. A* **95**, 042330 (2017).
- [47] G. Engelhardt, M. Benito, G. Platero, and T. Brandes, Topologically Enforced Bifurcations in Superconducting Circuits, *Phys. Rev. Lett.* **118**, 197702 (2017).
- [48] L. S. Levitov, T. P. Orlando, J. B. Majer, and J. E. Mooij, Quantum spin chains and Majorana states in arrays of coupled qubits, *Quantum* **3**, 7 (2001).
- [49] L. Tian, Circuit QED and Sudden Phase Switching in a Superconducting Qubit Array, *Phys. Rev. Lett.* **105**,

- 167001 (2010).
- [50] M. W. Johnson, M. H. S. Amin, S. Gildert, T. Lanting, F. Hamze, N. Dickson, R. Harris, A. J. Berkley, J. Johansson, P. Bunyk, E. M. Chapple, C. Enderud, J. P. Hilton, K. Karimi, E. Ladizinsky, N. Ladizinsky, T. Oh, I. Perminov, C. Rich, M. C. Thom, E. Tolkacheva, C. J. S. Truncik, S. Uchaikin, J. Wang, B. Wilson, and G. Rose, Quantum annealing with manufactured spins, *Nature* **473**, 194 (2011).
- [51] O. Viehmann, J. von Delft, and F. Marquardt, Observing the Nonequilibrium Dynamics of the Quantum Transverse-Field Ising Chain in Circuit QED, *Phys. Rev. Lett.* **110**, 030601 (2013).
- [52] O. Viehmann, J. V. Delft, and F. Marquardt, The quantum transverse-field Ising chain in circuit quantum electrodynamics: effects of disorder on the nonequilibrium dynamics, *New J. Phys.* **15**, 035013 (2013).
- [53] P. G. Harper, Single Band Motion of Conduction Electrons in a Uniform Magnetic Field, *Proc. Phys. Soc. Sect. A* **68**, 874 (1955).
- [54] S. Aubry and G. André, Analyticity breaking and Anderson localization in incommensurate lattices, *Ann. Isr. Phys. Soc.* **3**, 133 (1980).
- [55] F. G. Paauw, A. Fedorov, C. J. P. M. Harmans, and J. E. Mooij, Tuning the Gap of a Superconducting Flux Qubit, *Phys. Rev. Lett.* **102**, 090501 (2009).
- [56] F. Paauw, *Superconducting flux qubits: Quantum chains and tunable qubits*, Ph.D. thesis, Delft University of Technology (2009).
- [57] M. J. Schwarz, J. Goetz, Z. Jiang, T. Niemczyk, F. Deppe, A. Marx, and R. Gross, Gradiometric flux qubits with a tunable gap, *New J. Phys.* **15**, 045001 (2013).
- [58] X. Zhu, A. Kemp, S. Saito, and K. Semba, Coherent operation of a gap-tunable flux qubit, *Appl. Phys. Lett.* **97**, 102503 (2010).
- [59] Y.-x. Liu, L. F. Wei, J. S. Tsai, and F. Nori, Controllable Coupling between Flux Qubits, *Phys. Rev. Lett.* **96**, 067003 (2006).
- [60] Y.-X. Liu, L. F. Wei, J. R. Johansson, J. S. Tsai, and F. Nori, Superconducting qubits can be coupled and addressed as trapped ions, *Phys. Rev. B* **76**, 144518 (2007).
- [61] M. Grajcar, Y.-X. Liu, F. Nori, and A. M. Zagoskin, Switchable resonant coupling of flux qubits, *Phys. Rev. B* **74**, 172505 (2006).
- [62] C. Rigetti, A. Blais, and M. H. Devoret, Protocol for Universal Gates in Optimally Biased Superconducting Qubits, *Phys. Rev. Lett.* **94**, 240502 (2005).
- [63] P. Bertet, C. J. P. M. Harmans, and J. E. Mooij, Parametric coupling for superconducting qubits, *Phys. Rev. B* **73**, 064512 (2006).
- [64] A. O. Niskanen, Y. Nakamura, and J.-S. Tsai, Tunable coupling scheme for flux qubits at the optimal point, *Phys. Rev. B* **73**, 094506 (2006).
- [65] T. Hime, P. A. Reichardt, B. L. T. Plourde, T. L. Robertson, C.-E. Wu, A. V. Ustinov, and J. Clarke, Solid-State Qubits with Current-Controlled Coupling, *Science* **314**, 1427 (2006).
- [66] A. O. Niskanen, K. Harrabi, F. Yoshihara, Y. Nakamura, S. Lloyd, and J. S. Tsai, Quantum Coherent Tunable Coupling of Superconducting Qubits, *Science* **316**, 723 (2007).
- [67] R. Harris, A. J. Berkley, M. W. Johnson, P. Bunyk, S. Govorkov, M. C. Thom, S. Uchaikin, A. B. Wilson, J. Chung, E. Holtham, J. D. Biamonte, A. Y. Smirnov, M. H. S. Amin, and A. Maassen van den Brink, Sign- and Magnitude-Tunable Coupler for Superconducting Flux Qubits, *Phys. Rev. Lett.* **98**, 177001 (2007).
- [68] S. H. W. van der Ploeg, A. Izmailkov, A. M. van den Brink, U. Hübner, M. Grajcar, E. Il'ichev, H.-G. Meyer, and A. M. Zagoskin, Controllable Coupling of Superconducting Flux Qubits, *Phys. Rev. Lett.* **98**, 057004 (2007).
- [69] M. S. Allman, F. Altomare, J. D. Whittaker, K. Cicak, D. Li, A. Sirois, J. Strong, J. D. Teufel, and R. W. Simmonds, Rf-SQUID-Mediated Coherent Tunable Coupling between a Superconducting Phase Qubit and a Lumped-Element Resonator, *Phys. Rev. Lett.* **104**, 177004 (2010).
- [70] R. C. Bialczak, M. Ansmann, M. Hofheinz, M. Lenander, E. Lucero, M. Neeley, A. D. O'Connell, D. Sank, H. Wang, M. Weides, J. Wenner, T. Yamamoto, A. N. Cleland, and J. M. Martinis, Fast Tunable Coupler for Superconducting Qubits, *Phys. Rev. Lett.* **106**, 060501 (2011).
- [71] T. P. Orlando, J. E. Mooij, L. Tian, C. H. van der Wal, L. S. Levitov, S. Lloyd, and J. J. Mazo, Superconducting persistent-current qubit, *Phys. Rev. B* **60**, 15398 (1999).
- [72] Y.-X. Liu, J. Q. You, L. F. Wei, C. P. Sun, and F. Nori, Optical selection rules and phase-dependent adiabatic state control in a superconducting quantum circuit, *Phys. Rev. Lett.* **95**, 087001 (2005).
- [73] J. Koch, T. M. Yu, J. M. Gambetta, A. A. Houck, D. I. Schuster, J. Majer, A. Blais, M. H. Devoret, S. M. Girvin, and R. J. Schoelkopf, Charge-insensitive qubit design derived from the Cooper pair box, *Phys. Rev. A* **76**, 042319 (2007).
- [74] R. Barends, J. Kelly, A. Megrant, D. Sank, E. Jeffrey, Y. Chen, Y. Yin, B. Chiaro, J. Y. Mutus, C. Neill, P. O'Malley, P. Roushan, J. Wenner, T. C. White, A. N. Cleland, and J. M. Martinis, Coherent Josephson qubit suitable for scalable quantum integrated circuits, *Phys. Rev. Lett.* **111**, 080502 (2013).
- [75] Y. Chen, C. Neill, P. Roushan, N. Leung, M. Fang, R. Barends, J. Kelly, B. Campbell, Z. Chen, B. Chiaro, A. Dunsworth, E. Jeffrey, A. Megrant, J. Y. Mutus, P. J. J. O'Malley, C. M. Quintana, D. Sank, A. Vainsencher, J. Wenner, T. C. White, M. R. Geller, A. N. Cleland, and J. M. Martinis, Qubit Architecture with High Coherence and Fast Tunable Coupling, *Phys. Rev. Lett.* **113**, 220502 (2014).
- [76] M. R. Geller, E. Donate, Y. Chen, M. T. Fang, N. Leung, C. Neill, P. Roushan, and J. M. Martinis, Tunable coupler for superconducting Xmon qubits: Perturbative nonlinear model, *Phys. Rev. A* **92**, 012320 (2015).
- [77] A. Fedorov, A. K. Feofanov, P. Macha, P. Forn-Díaz, C. J. P. M. Harmans, and J. E. Mooij, Strong Coupling of a Quantum Oscillator to a Flux Qubit at Its Symmetry Point, *Phys. Rev. Lett.* **105**, 060503 (2010).
- [78] E. Fradkin, *Field Theories of Condensed Matter Physics*, 2nd ed. (Cambridge University Press, 2013).
- [79] M. J. Rice and E. J. Mele, Elementary Excitations of a Linearly Conjugated Diatomic Polymer, *Phys. Rev. Lett.* **49**, 1455 (1982).
- [80] G. Wanner and E. Hairer, *Solving ordinary differential equations II*, Vol. 375 (Springer Berlin Heidelberg, 1996).
- [81] S. Longhi, G. L. Giorgi, and R. Zambrini, Landau–

- zener topological quantum state transfer, *Adv. Quantum Technol.* **2**, 1800090 (2019).
- [82] Z.-G. Chen, W. Tang, R.-Y. Zhang, Z. Chen, and G. Ma, Landau-Zener Transition in the Dynamic Transfer of Acoustic Topological States, *Phys. Rev. Lett.* **126**, 054301 (2021).
- [83] Y.-X. Shen, L.-S. Zeng, Z.-G. Geng, D.-G. Zhao, Y.-G. Peng, J. Zhu, and X.-F. Zhu, Acoustic topological adiabatic passage via a level crossing, *Sci. China: Phys. Mech. Astron.* **64**, 1 (2021).
- [84] L. D. Landau and E. M. Lifshitz, *Quantum mechanics: non-relativistic theory*, Vol. 3 (Elsevier, 1977).
- [85] L. P. Yatsenko, S. Guérin, and H. R. Jauslin, Topology of adiabatic passage, *Phys. Rev. A* **65**, 043407 (2002).
- [86] A. Messiah, *Quantum mechanics: volume II* (North-Holland Publishing Company Amsterdam, 1962).
- [87] M. V. Berry, Quantal phase factors accompanying adiabatic changes, *Proc. Math. Phys. Eng. Sci.* **392**, 45 (1984).
- [88] A. Anastasiadis, G. Styliaris, R. Chaunsali, G. Theocharis, and F. K. Diakonov, Bulk-edge correspondence in the trimer Su-Schrieffer-Heeger model, *Phys. Rev. B* **106**, 085109 (2022).
- [89] H. Paik, D. I. Schuster, L. S. Bishop, G. Kirchmair, G. Catelani, A. P. Sears, B. R. Johnson, M. J. Reagor, L. Frunzio, L. I. Glazman, S. M. Girvin, M. H. Devoret, and R. J. Schoelkopf, Observation of High Coherence in Josephson Junction Qubits Measured in a Three-Dimensional Circuit QED Architecture, *Phys. Rev. Lett.* **107**, 240501 (2011).
- [90] S. Novikov, T. Sweeney, J. E. Robinson, S. P. Premaratne, B. Suri, F. C. Wellstood, and B. S. Palmer, Raman coherence in a circuit quantum electrodynamics lambda system, *Nat. Phys.* **12**, 75 (2016).
- [91] W. Cai, J. Han, F. Mei, Y. Xu, Y. Ma, X. Li, H. Wang, Y. P. Song, Z.-Y. Xue, Z.-q. Yin, S. Jia, and L. Sun, Observation of Topological Magnon Insulator States in a Superconducting Circuit, *Phys. Rev. Lett.* **123**, 080501 (2019).
- [92] A. M. Deac, A. Fukushima, H. Kubota, H. Maehara, Y. Suzuki, S. Yuasa, Y. Nagamine, K. Tsunekawa, D. D. Djayaprawira, and N. Watanabe, Bias-driven high-power microwave emission from MgO-based tunnel magnetoresistance devices, *Nat. Phys.* **4**, 803 (2008).
- [93] B. Béri, Topologically stable gapless phases of time-reversal-invariant superconductors, *Phys. Rev. B* **81**, 134515 (2010).
- [94] G. Romero, J. J. García-Ripoll, and E. Solano, Microwave Photon Detector in Circuit QED, *Phys. Rev. Lett.* **102**, 173602 (2009).
- [95] F. Mallet, F. R. Ong, A. Palacios-Laloy, F. Nguyen, P. Bertet, D. Vion, and D. Esteve, Single-shot qubit readout in circuit quantum electrodynamics, *Nat. Phys.* **5**, 791 (2009).
- [96] L.-J. Lang, X. Cai, and S. Chen, Edge States and Topological Phases in One-Dimensional Optical Superlattices, *Phys. Rev. Lett.* **108**, 220401 (2012).
- [97] D. R. Hofstadter, Energy levels and wave functions of Bloch electrons in rational and irrational magnetic fields, *Phys. Rev. B* **14**, 2239 (1976).
- [98] Y. E. Kraus, Y. Lahini, Z. Ringel, M. Verbin, and O. Zeitlinger, Topological States and Adiabatic Pumping in Quasicrystals, *Phys. Rev. Lett.* **109**, 106402 (2012).
- [99] P. Roushan, C. Neill, J. Tangpanitanon, V. M. Bastidas, A. Megrant, R. Barends, Y. Chen, Z. Chen, B. Chiaro, A. Dunsworth, A. Fowler, B. Foxen, M. Giustina, E. Jeffrey, J. Kelly, E. Lucero, J. Mutus, M. Neeley, C. Quintana, D. Sank, A. Vainsencher, J. Wenner, T. White, H. Neven, D. G. Angelakis, and J. Martinis, Spectroscopic signatures of localization with interacting photons in superconducting qubits, *Science* **358**, 1175 (2017).
- [100] L. Zhou, S. Yang, Y.-x. Liu, C. P. Sun, and F. Nori, Quantum Zeno switch for single-photon coherent transport, *Phys. Rev. A* **80**, 062109 (2009).
- [101] Y.-x. Liu, C.-X. Yang, H.-C. Sun, and X.-B. Wang, Coexistence of single- and multi-photon processes due to longitudinal couplings between superconducting flux qubits and external fields, *New J. Phys.* **16**, 015031 (2014).
- [102] P.-M. Billangeon, J. S. Tsai, and Y. Nakamura, Circuit-QED-based scalable architectures for quantum information processing with superconducting qubits, *Phys. Rev. B* **91**, 094517 (2015).
- [103] J. Goetz, F. Deppe, K. G. Fedorov, P. Eder, M. Fischer, S. Pogorzalek, E. Xie, A. Marx, and R. Gross, Parity-Engineered Light-Matter Interaction, *Phys. Rev. Lett.* **121**, 060503 (2018).
- [104] Y. Wang, Y. Li, Z.-q. Yin, and B. Zeng, 16-qubit IBM universal quantum computer can be fully entangled, *Npj Quantum Inf.* **4**, 1 (2018).
- [105] X. Li, Y. Ma, J. Han, T. Chen, Y. Xu, W. Cai, H. Wang, Y. Song, Z.-Y. Xue, Z.-q. Yin, and L. Sun, Perfect Quantum State Transfer in a Superconducting Qubit Chain with Parametrically Tunable Couplings, *Phys. Rev. Appl.* **10**, 054009 (2018).
- [106] Y.-x. Liu, L. F. Wei, and F. Nori, Measuring the quality factor of a microwave cavity using superconducting qubit devices, *Phys. Rev. A* **72**, 033818 (2005).
- [107] M. P. Estarellas, I. D'Amico, and T. P. Spiller, Topologically protected localised states in spin chains, *Sci. Rep.* **7**, 42904 (2017).
- [108] S. Bose, Quantum Communication through an Unmodulated Spin Chain, *Phys. Rev. Lett.* **91**, 207901 (2003).
- [109] M. H. Devoret, Quantum fluctuations in electrical circuits, *Les Houches, Sess. LXIII* (1995).
- [110] G. Wendin and V. S. Shumeiko, Superconducting Quantum Circuits, Qubits and Computing, *arXiv preprint cond-mat/0508729* (2005).